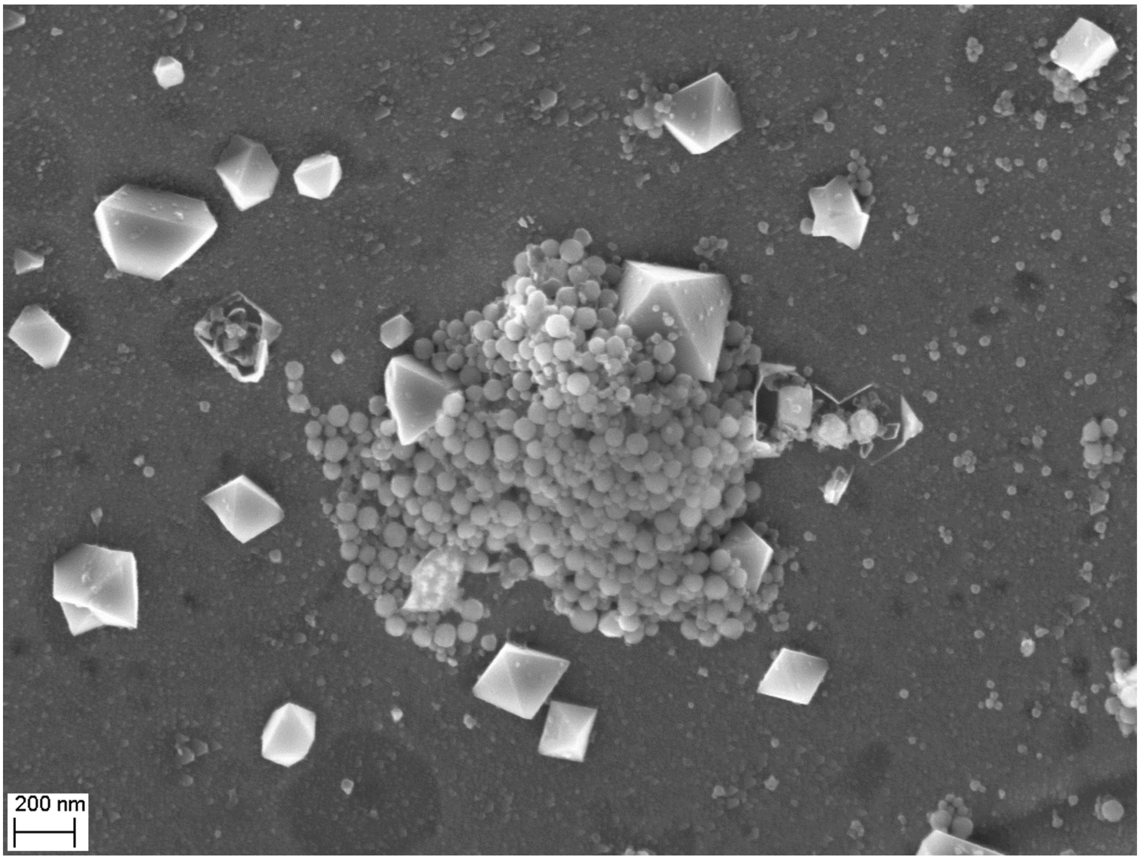

Structural Characterization of Oxide Films Formed on Stainless Steel of Type 304L in Simulated PWR Primary Water

Master's Thesis in Applied Physics

CECILIA FAGER

Department of Applied Physics
Division of Materials Microstructure
CHALMERS UNIVERSITY OF TECHNOLOGY
Gothenburg, Sweden 2015

Structural Characterization of Oxide Films Formed on Stainless Steel of Type 304L in Simulated PWR Primary Water

CECILIA FAGER

Department of Applied Physics
Chalmers University of Technology
Gothenburg, 2015

Structural Characterization of Oxide Films Formed on Stainless Steel of Type 304L in Simulated PWR Primary Water

CECILIA FAGER

Department of Applied Physics
Chalmers University of Technology
SE-412 96 Gothenburg
Sweden
Telephone: +46 (0)31 772 10 00

Cover shows a SEM SE micrograph of precipitated oxide crystals and spherical oxide particles formed on stainless steel of type 304L exposed in simulated PWR hot leg environment.

Structural Characterization of Oxide Films Formed on Stainless Steel of Type 304L in Simulated PWR Primary Water

CECILIA FAGER
Department of Applied Physics
Chalmers University of Technology

ABSTRACT

Many different materials are used in Pressurized Water Reactors (PWR). In PWR high temperature high pressure corrosive environments a part of the corrosion products of these materials would release into the reactor coolant, some of which may get neutron activated to form a variety of radionuclides. The radionuclides, in the form of either solids or dissolved chemical species, circulate in reactor circuits and can deposit onto the oxide films being formed on the metal surfaces, leading to activity build-up in the plant and thus increases the dose rate. Zinc injection is known to be capable of reducing the corrosion rate of reactor materials and the activity build-up and is therefore being increasingly implemented in light water reactors worldwide. However, the fundamental mechanism behind the effects of zinc has not yet been fully understood.

In this work the oxide films formed on three test coupons of stainless steel of type 304L that had been exposed to simulated PWR primary water conditions have been examined. Each test coupon had been subjected to different exposure environments such as with or without zinc injection, and Co-60 radiotracer was used to measure activity deposition rates under various water chemistry conditions.

In order to understand the different activity deposition rates on the three test coupons, a structural characterization has been carried out using X-Ray Powder Diffraction (XRD), Laser Raman Spectroscopy (LRS), Scanning Electron Microscopy (SEM), equipped with Energy Dispersive X-ray Spectroscopy (EDS) and Focused Ion Beam (FIB), and High Resolution Analytical Transmission Electron Microscopy (HR ATEM). The presence of spinel phase (Me_3O_4) in all oxide films has been confirmed by the XRD and partly also by the LRS measurements. High resolution SEM topography examinations have revealed two kinds of surface oxide grains, (1) relatively large Fe-rich oxide crystals of regular shapes being sparsely distributed on the corroded surfaces, (2) tiny spherical Si-rich oxides which formed agglomerates locally. Cross-section examination with the FIB/SEM technique has revealed a thin oxide film, with a thickness of approximately 10 nm, inward growing crater oxides, with depth of approximately 200 nm, that were present beneath surface oxide grains. High resolution micrographs of the oxide films and zinc concentration profiles across the thin oxide films have also been obtained with HR ATEM. Combined with the present experimental findings the Point Defect Model (PDM) as developed by Macdonald has been used to explain the inhibition effect on the Co-60 incorporation in the oxide films by zinc injection. Suggestions for future work are also proposed.

Keywords: PWR, SS304L, XRD, LRS, SEM, TEM, EDS

TABLE OF CONTENTS

LIST OF FIGURES

LIST OF TABLES

LIST OF ABBREVATIONS

PWR	Pressurized Water Reactor
SS 304L	Stainless Steel 304L
XRD	X-Ray powder Diffraction
LRS	Laser Raman Spectroscopy
SEM	Scanning Electron Microscopy
FIB	Focused Ion Beam
TEM	Transmission Electron Microscopy
EDS	Energy Dispersive x-ray Spectroscopy

1. INTRODUCTION

1.1 BACKGROUND

A variety of materials are used in nuclear Pressurized Water Reactors (PWR), all of which must be able to withstand corrosive aqueous environment. In PWR high temperature, high pressure corrosive environments, parts of the corrosion products of these materials are released into the reactor coolant, some of which may get neutron activated and forming a variety of radionuclides [1]. The radionuclides, in the form of either solids or dissolved chemical species, circulate in the reactor circuits and can deposit onto the oxide films being formed on the metal surfaces, leading to activity build-up in the plant and thus increases the dose rate. An elevated dose rate in the plant presents both a health risk to service personnel and is also costly to remedy for plant operators, as some of these radioactive species, such as Co-58 and Co-60 with relatively long half-life of 72 days and 5.3 years, respectively [2], are persistent and difficult to remove.

In PWR steam generators, where stainless steel of type 304L is used in components, the relatively high radioactivity build-up and the resulting dose rate is a matter of great concern. It is therefore of great interest to investigate how to control and to decrease the activity build-up on these components through optimized water chemistry management. For example, zinc injection is an increasingly applied technique to remedy the radioactivity build-up problem in the PWR’s primary circuit. But the mechanism behind this desired effect has not yet been fully understood.

For this purpose, a large research effort initiated by Ringhals nuclear power plant is devoted to examining the effect of various water chemistry parameters, including coolant temperature and pH as well as zinc injection. This thesis work is a part of the overall effort and partly financed by Ringhals nuclear power plant.

1.2 AIM OF MASTER THESIS

The aim of this master thesis is to *explore the inhibition effect on the Co-60 incorporation in the oxide films by zinc injection.* This aim is pursued through performing structural characterization of the formed oxide films on three test coupons of stainless steel of type 304L having been exposed under different water chemistry conditions at PWR hot leg coolant temperature and interpreting the findings with the Point Defect Model (PDM), as developed by Macdonald [3].

1.3 THESIS SCOPE

Autoclave exposure experiments were performed by Studsvik Nuclear AB under contract with Ringhals nuclear power plant. The test coupons, including three prepared TEM-lamellas were made available by Studsvik Nuclear AB to this work. Based on the experimental findings in this work, PDM is applied to explain the inhibition effect on the Co-60 incorporation in the oxide films by zinc injection. Hence, the scope of the thesis is to perform structural characterization on the oxide films on the test coupons based on which PDM is applied to elucidate the possible mechanism of the inhibition effect on Co-60 incorporation in the oxide films by zinc injection.

1.4 OUTLINE OF MASTER THESIS

After this introductory chapter, chapter 2 introduces the reader to the concept of Pressurized Water Reactors (PWR) and the water chemistry conditions under which the test coupons used in this work were exposed. The characteristics of stainless steel of type 304L, used in PWRs and examined in this work, are also presented. Chapter 3 then presents some previous studies on characterization of oxide films formed on similar materials. In Chapter 4, PDM as developed by Macdonald, is briefly described [3]. Chapter 5 includes descriptions of all analytical techniques and some key operating parameters used in the measurements. Chapter 6 describes the studied material and test rig for the autoclave exposure and water chemistry conditions applied, including the main result from the tracer study performed by Studsvik Nuclear AB. In Chapter 7, the main results are presented, analysed and discussed. Chapter 8 presents the conclusions of this study. Finally, chapter 9 outlines some suggestions for further work.

2. PWR, STAINLESS STEEL AND WATER CHEMISTRY

2.1 PRESSURIZED WATER REACTOR

A pressurized water reactor (PWR) involves a primary water circuit and a secondary water circuit. Figure 1 is a schematic drawing of a PWR and a detailed description about the operational processes can be found elsewhere [4, 5]. In the following a brief description is presented.

The water in the primary circuit passes through the reactor vessel where it is heated to a temperature of approximately 300 °C by energy that is released during fission reactions. The control rods are used to regulate the fission reactions. The purpose of the pressurizer is to prevent the water from boiling. The heated primary water then passes through the steam generators, where heat transfer between the primary circuit and the secondary circuit occurs and primary water temperature drops accordingly. The cooler primary water is then pumped back into the reactor vessel. The transferred heat causes the secondary circuit water to boil and thus creating water vapour that is further used to drive the turbine, which will generate electricity since a generator is connected. Cooling water is used in the condenser to condense the water vapour to liquid and then pump back the secondary water to the steam generator again.

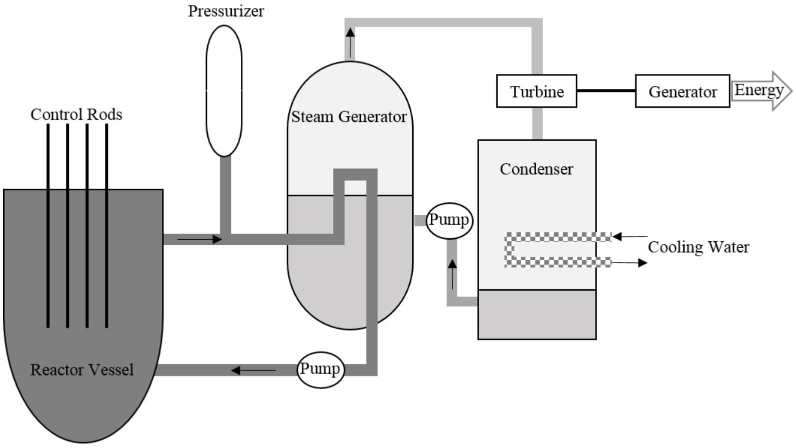

Figure 1 - Illustration of a Pressurized Water Reactor (PWR), where the dark grey tubes indicate the primary water circuit and the lighter grey tubes indicate the secondary water circuit. After reference [5].

2.2 STAINLESS STEEL MATERIALS USED IN STEAM GENERATORS

Stainless steels and nickel based alloys are two common materials used in PWR primary water circuits [6]. The definition of stainless steel is an alloy containing most part of iron with a chromium content of at least 10.5 wt-% [7]. One type of stainless steel is the austenitic stainless steel which have a face-centred cubic crystal structure.

The purpose of adding nickel and manganese as alloying elements is that they have an austenitic stabilizing function. The austenite phase fulfils many of the mechanical properties such as good toughness, that are desired from a stainless steel material [8]. For example, some parts of the steam generators are made of austenitic stainless steel of type 304L (denoted SS 304L in the following), where the designation L indicates low carbon content [9].

2.3 WATER CHEMISTRY

In PWR primary water small quantities of boron acid and lithium hydroxide are added. The purpose of adding boric acid is because boron enables controlling of the reactor power [10], while adding lithium reduces the corrosion rate of the materials through increasing the coolant pH. In the following chapter, some previous studies regarding radioactivity build-up in oxide films are presented, in which the effects of some operating parameters, such as coolant pH, temperature, flowrate and zinc addition, on activity build-up were examined.

3. RADIOACTIVITY BUILD-UP IN STEAM GENERATORS

In a light water nuclear reactor core, fission reactions occur between neutrons and, for example, Uranium-235 nucleus. These emitted neutrons due to chain reactions may hit everything in their way including corrosion products of various reactor materials in reactor coolant circuits [10]. Some of the corrosion products deposit on fuel surfaces and form a solid deposit called fuel CRUD. By neutron activation and other nuclear reactions some elements of fuel CRUD will become highly radioactive radionuclides, for example, cobalt becomes Co-60 and nickel becomes Co-58. Fuel CRUD may release into reactor coolant, in forms of solid particles and dissolved species, causing activity deposition on the surfaces of various reactor components. The solid radioactive species may deposit as so-called *hot spots* on the metal surfaces, while the dissolved radioactive species in the coolant may react with the oxide films being formed on the material surfaces and get incorporated. Both deposition processes would contribute to plant radiation field build-up.

3.1 PREVIOUS WORK

3.1.1 RINGHALS PWR DOSE RATE PROBLEMATIC

Bengtsson, et al. [11] studied the steam generator dose rate development in Ringhals 3 PWR units between 2000 and 2008 and the results of operating unit 2 and 3 under elevated lithium chemistry conditions (lithium level at 3.5 ppm or higher and pH value of 7.4 at 300 °C). They compared the results with, among others, that of unit 4 where the pH at 300 °C was kept at 7.25. Generally one could see that the cold leg dose rate decreased considerably following the introduction of the elevated lithium chemistry and got closer to the hot leg dose rate over time.

As the change to the elevated lithium chemistry was accompanied by the change of steam generator tubing material from Alloy 600 to much more corrosion resistant Alloy 690, it is not possible to attribute the observed dose rate reduction solely to the elevated lithium chemistry. One may argue that the observed dose rate reduction could be the result of overall reduction of radioactive source term because of the use of more corrosion resistant Alloy 690.

3.1.2 RESULTS OF LABORATORY SIMULATION OF ACTIVITY BUILD-UP

Under the contract with Ringhals nuclear power plant, Studsvik has performed several laboratory autoclave exposures in which water chemistry conditions under different reactor operating modes were simulated and the activity build-up on both corroding SS 304L and Alloy 690 materials was examined using radiotracer Co-60 [12]. In these experiments various operating parameters such as elevated lithium chemistry, zinc injection, coolant temperature, start-up and shutdown operation as well as hydrogen peroxide injection were simulated in order to see how the activity deposition rate was affected by each parameter. Among many interesting experimental observations, the followings are noteworthy:

1) Activity buildup rate was largely constant over time under a given water chemistry condition.
2) Activity buildup rate decreased instantaneously with increasing zinc concentration from 0 to 5 or 10 ppb in coolant and vice versa, and reached rapidly a constant rate at a given zinc concentration.
3) Activity buildup rate was not dependent on primary coolant $pH_{T.}$
4) Upon a stop in Co-60 injection, the previously deposited Co-60 activity on the material surfaces would release. Such a release was accelerated when zinc was added to the coolant.
5) The stainless steel test section at the lower part of each test leg had a deposition rate of approximately 50% of the stainless steel section at the upper part, although approximately 90% of coolant Co-60 passed the test section.
6) Simulated acid oxidizing shutdown (with injection of H_2O_2 at 85 °C) did not remove any significant deposited activity on the material surfaces.

Without a proper knowledge of the oxide film microstructures and good understanding about the mass transport processes occurring in the oxide films during the exposures, it is not possible to explain the results obtained from the radiotracer experiments as mentioned above.

3.1.3 CHARACTERIZATION OF OXIDE FILM FORMED ON STAINLESS STEELS

A previous work concerning characterization of oxide films formed on SS 304 are presented by Liu, et al. [13] using X-ray Photoelectron Spectroscopy (XPS). In this work a SS 304 material was exposed in borated and lithiated high temperature water (with 2.3 ppm lithium from $LiOH \cdot H_2O$, 1500 ppm B from H_3BO_3 and 10 ppb zinc from ZnO in the case of zinc injection) up to 20 days at temperature of 300 °C with and without presence of zinc. Without zinc addition, the formed oxide films were composed of a spinel oxide mixture of Fe_3O_4 and $FeCr_2O_4$, while with zinc addition the oxide films consisted of $ZnFe_2O_4$ and $ZnCr_2O_4$. Furthermore, with zinc addition, the thickness of the oxide films were significantly thinner than that when no zinc was added. In the latter case, the formed $ZnCr_2O_4$ became the dominant phase in the formed oxide film after a long exposure.

Tapping, et al. [14] used Scanning Auger Microscopy (SAM) and Scanning Electron Microscopy (SEM) to study the morphology and compositions of the oxide films formed on a SS 304L at 300 °C and pH 10.3 after 576 hours in lithiated high temperature water. The corroded surfaces had an oxide film of duplex structure, with an outer layer consisting of a Fe-rich crystalline oxides and an inner layer of Cr-rich oxide.

4. THEORETICAL ASPECTS OF CORROSION MECHANISM

4.1 POINT DEFECT MODEL

PDM is a model that describes metal corrosion mechanism in aqueous environment [3]. It is originated from an attempt to apply the Wagner's theory, which is a theory describing the growth of oxide film in absence of aqueous environment, to the growth of oxide film when an aqueous environment is present.

There are three generations of this model, PDM-I is the first generation, and PDM-II is an improved version of PDM-I. One of the major improvements from PDM-I to PDM-II is that it considers dissolution of the oxide film, which allows a steady state of the oxide film to be reached. The third generation of PDM, PDM-III, would also consider the effect of forming a dense outer oxide layer and is still under development. Concerning the studied material in this thesis, PDM-II is probably the most relevant model for suggesting possible routes for radioactive cobalt and zinc species in the primary water to be deposited on the surface or incorporated in the oxide films. In Figure 2, various reactions occurring at the metal/oxide interface and oxide/solution interface, according to PDM-II, are presented [3].

With this model, several assumptions are made. Passive films generally form as bi-layers with an inner (barrier) layer containing elements that are only present in the metal substrate and an outer (precipitated) layer containing species present in the barrier layer and the aqueous solution. Some other assumptions and postulates include:

- The inner layer comprises a point defective crystalline lattice with the dominant point defects being cation vacancies, cation interstitials and oxygen vacancies. The point defects determine the electronic character of the film. This layer grows directly into the metal.
- The outer layer forms via precipitation due to hydrolysis of cations originated from the barrier layer.
- The defects are generated and annihilated continuously at the metal/film (m/f) and film/solution (f/s) interfaces with each interface acting as either a source or a sink for the defects.
- The electric field strength is independent of voltage and distance through the film, implying that the rate control resides at the metal/barrier layer interface.
- Dissolution of the barrier layer is a chemical or electrochemical process that allows the oxide film thickness and the current to achieve steady state.
- The interfacial reactions are classified as to whether they are lattice non-conservative (i.e. they result in movement of the boundaries upon their occurrence) or lattice conservative (i.e. they do not result in movement of the boundaries upon their occurrence).

Several defect chemistry reactions that occurs when a metal surface is exposed to an aqueous environment according to PDM-II are illustrated in Figure 2 and the notions used are explained as followed [3].

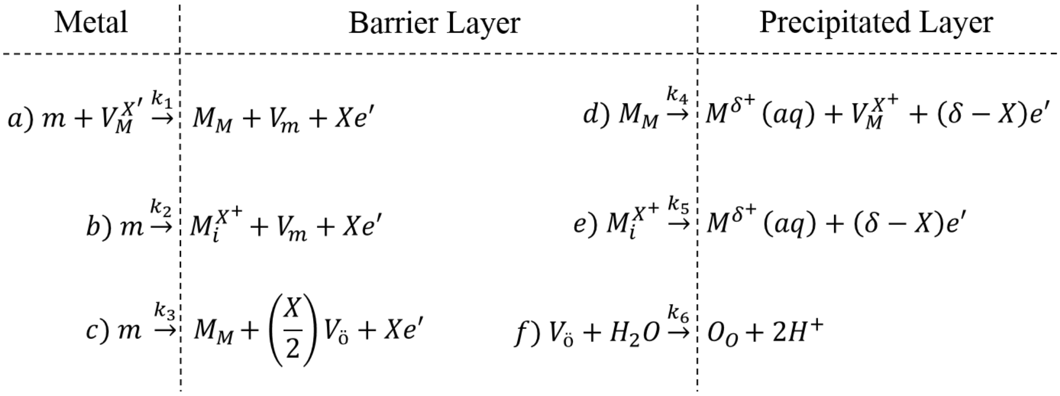

$$a)\ m + V_M^{X'} \xrightarrow{k_1} M_M + V_m + Xe' \qquad d)\ M_M \xrightarrow{k_4} M^{\delta+}(aq) + V_M^{X+} + (\delta - X)e'$$

$$b)\ m \xrightarrow{k_2} M_i^{X+} + V_m + Xe' \qquad e)\ M_i^{X+} \xrightarrow{k_5} M^{\delta+}(aq) + (\delta - X)e'$$

$$c)\ m \xrightarrow{k_3} M_M + \left(\frac{X}{2}\right) V_{\ddot{o}} + Xe' \qquad f)\ V_{\ddot{o}} + H_2O \xrightarrow{k_6} O_O + 2H^+$$

Figure 2 - Summary of the defect generation and annihilation reactions envisioned to occur at the interfaces of the barrier layer on a metal surface. m: Cation on a metal substrate lattice site, V_m cation vacancy in the metal substrate, M_M cation in cation site on the cation sublattice, $V_M^{X'}$ cation vacancy, M_i^{X+} cation interstitial, O_O oxide ion in anion site on the anion sublattice, $V_O^{\cdot\cdot}$ anion vacancy in the barrier layer, $M^{\delta+}$ (aq) cation in the outer layer/solution interface precipitated layer and $MO_{X/2}$ stoichiometric barrier layer oxide. Note that Reactions a, b, d, e and f are lattice conservative processes, whereas Reactions c and g are non-conservative.
After reference [3].

The addition of reactions a), b), d) and e) corresponds to metal dissolution. These reactions are independent of the barrier layer, with the barrier layer simply acting as a semi-permeable membrane. The addition of reactions c) and g) corresponds to growth of the barrier layer. An important conclusion from this model is that the barrier layer contains only those species that are present in the metal and not those species in the aqueous solution. The formation of the outer layer can occur by hydrolysis of cations transmitted through the barrier layer, reaction involving anions present in the solution or by reaction of the barrier layer at the barrier layer/precipitated layer interface with the aqueous solution. Being dependent of substrate materials and environments, the outer oxide layer may consist of oxides, oxyhydroxides and hydroxides or more mixed species.

4.1.1 POINT DEFECT MODEL CONSIDERING ZINC

An attempt has been made by Wu, et al. [13] to explain the occurring corrosion reactions of SS 304L when zinc is present in aqueous environment. They added 3 more reactions involving zinc species to those in PDM-II (reactions h, i and j in Figure 3). As already mentioned, only lattice non-conservative reactions can cause either growth or dissolution of the oxide film. In the present case reaction c, g and j are of these types of reactions. In this modified model, however, the presence of radioactive cobalt and other species in the solution is not considered. The model case that considers both Co^{2+} (aq) and Zn^{2+} (aq) will be discussed in Chapter 7.5.

Some precautions were mentioned by Macdonald et al. [3] regarding the use of some analytical techniques that work under ultrahigh vacuum (UHV) condition. When transferring a sample from ambient conditions to high vacuum systems there might be a change such as dehydration of hydroxides and oxyhydroxides into oxyhydroxides and oxides, respectively. This possibility should be taken into account when examining and interpreting the data from this microscopy study.

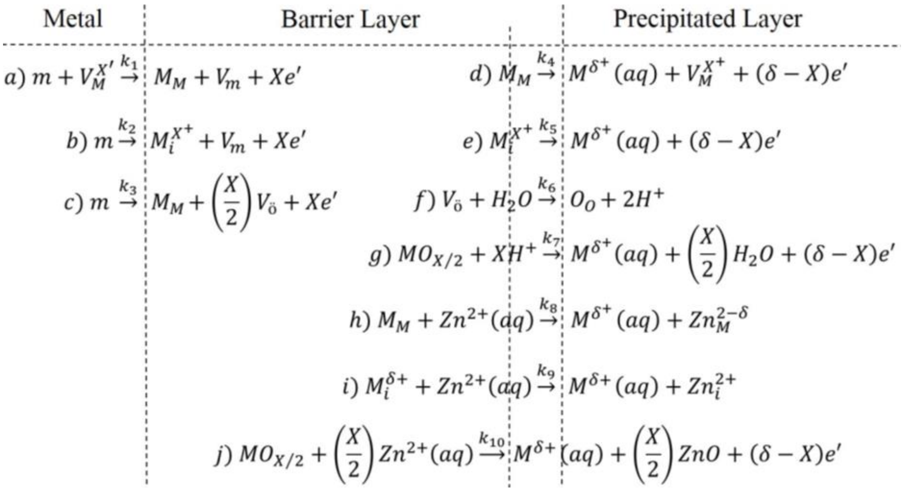

$$a)\ m + V_M^{X'} \xrightarrow{k_1} M_M + V_m + Xe'$$

$$b)\ m \xrightarrow{k_2} M_i^{X+} + V_m + Xe'$$

$$c)\ m \xrightarrow{k_3} M_M + \left(\frac{X}{2}\right) V_{\ddot{o}} + Xe'$$

$$d)\ M_M \xrightarrow{k_4} M^{\delta+}(aq) + V_M^{X+} + (\delta - X)e'$$

$$e)\ M_i^{X+} \xrightarrow{k_5} M^{\delta+}(aq) + (\delta - X)e'$$

$$f)\ V_{\ddot{o}} + H_2O \xrightarrow{k_6} O_O + 2H^+$$

$$g)\ MO_{X/2} + XH^+ \xrightarrow{k_7} M^{\delta+}(aq) + \left(\frac{X}{2}\right) H_2O + (\delta - X)e'$$

$$h)\ M_M + Zn^{2+}(aq) \xrightarrow{k_8} M^{\delta+}(aq) + Zn_M^{2-\delta}$$

$$i)\ M_i^{\delta+} + Zn^{2+}(aq) \xrightarrow{k_9} M^{\delta+}(aq) + Zn_i^{2+}$$

$$j)\ MO_{X/2} + \left(\frac{X}{2}\right) Zn^{2+}(aq) \xrightarrow{k_{10}} M^{\delta+}(aq) + \left(\frac{X}{2}\right) ZnO + (\delta - X)e'$$

Figure 3 - Summary of the defect generation and annihilation reactions envisioned to occur at the interfaces of the barrier oxide layer on a metal with the consideration of zinc presence in solution. After reference [13].

5. ANALYTICAL TECHNIQUES

Several advanced analytical techniques have been applied to acquire structural information about the oxide films that have formed on the stainless steel coupons. In particular, X-Ray powder Diffraction, Laser Raman Spectroscopy, Scanning Electron Microscopy and Transmission Electron Microscopy have been used during this thesis work. In the following, the principles of these techniques will be briefly introduced and their applications to solving the dedicated issues regarding the oxide film structures will also be discussed.

5.1 X-RAY POWDER DIFFRACTION

X-ray powder diffraction (XRD) is, among its various applications, a common technique for phase identification in a powder sample [15]. The principle of XRD is that if Bragg's law is fulfilled, which it only is if constructive interference occurs, the x-rays will be diffracted and detected by an X-ray detector. Bragg's law is written as equation (1):

$$n\lambda = 2dsin\theta \tag{1}$$

Where n is an integer, λ is the wavelength of the incident x-ray (1.54060 Å as used in this XRD study), d is the distance between the atomic planes and θ is the angle of the incident x-rays. Constructive interference is achieved when the reflected beams *b* and *d* are in phase with each other, which is illustrated in Figure 4.

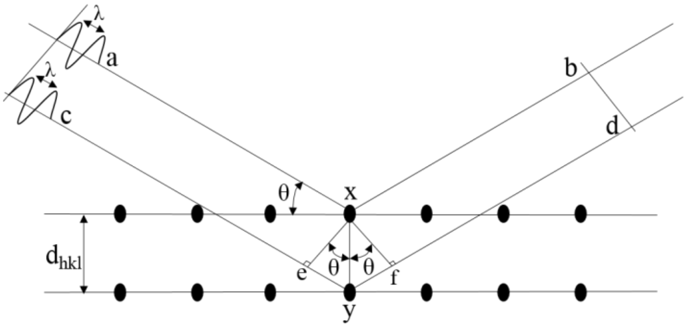

Figure 4 - Illustration of a crystal with the black dots illustrating the lattice points and the lines between the dots illustrating atomic planes with Miller indices hkl *and the atomic spacing d_{hkl}. The angle θ is the angle of the incident X-rays* ac *and the X-rays will be reflected by atom* x *and* y*, respectively. Constructive interference is achieved when the reflected beams* b *and* d *are in phase with each other. After reference [15].*

In the present work, the setup of the diffractometer, model D8 Advance from Bruker, is shown in Figure 5. The diffractometer was operated using θ/2θ scans at 45 kV and 40 mA, with 2θ ranging from 15° to 92° with a step size of 0.034°. For the present test coupons the diffracted peaks come from not only the oxide films but also from the metal substrate underneath due to the relatively deep penetration of X-ray beam in the operating mode. The measured data are compared with PDF (Powder Diffraction File) database using Diffrac.EVA for phase identification.

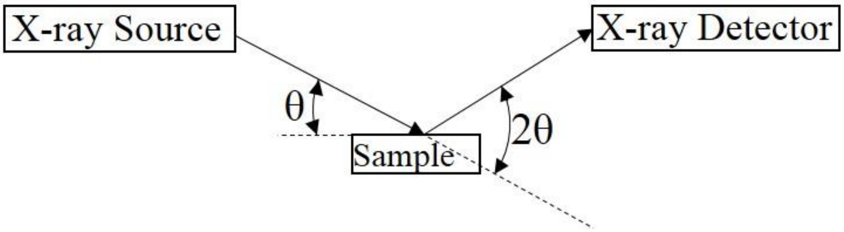

Figure 5 - Setup of a diffractometer with θ/2θ scan used in this work. After reference [15].

The measured XRD raw data were treated as the following. The background was then smoothened by a smooth factor of 0.256 to reduce background noise. To remove the data offset effect caused by the slight surface misalignment in each measurement, all diffracted peaks from the base metal were made to be in agreement with the literature data for SS 304L (PDF 00-033-0397) so that the diffracted peaks from oxide films could be compared between different phases in the same specimen or between different specimens in different XRD measurements.

Since different spinel phases have similar crystal structures, their diffracted peaks will appear at similar positions in a diffractogram. It makes the differentiation by XRD technique between different spinel phases difficult. Therefore, in case of coexistence of different spinel phases in the oxide films, other analytical techniques such as electron diffraction and composition analysis in TEM may be used.

5.2 LASER RAMAN SPECTROSCOPY

Laser Raman Spectroscopy (LRS) can be used for many purposes. One of them can be phase identification. The principle of LRS can be described briefly as the following. Figure 6 shows schematically the Rayleigh scattering (it occurs when the incident laser beam with frequency ν_i is scattered, after irradiating the sample, with the same frequency) and Raman Scattering (it occurs when the incident laser beam is scattered with another frequency after irradiating the sample, which is denoted ν_r) processes. A laser beam is often used in Raman measurements as it has enough energy to cause a transition of a molecule from one vibrational energy level to another [16, 17]. By determining the induced dipole moments caused by the interaction between the laser and the sample, and the resulting different excited vibrational energy levels in the sample one may obtain some chemical and structural information that would be specific or unique to a certain chemical species.

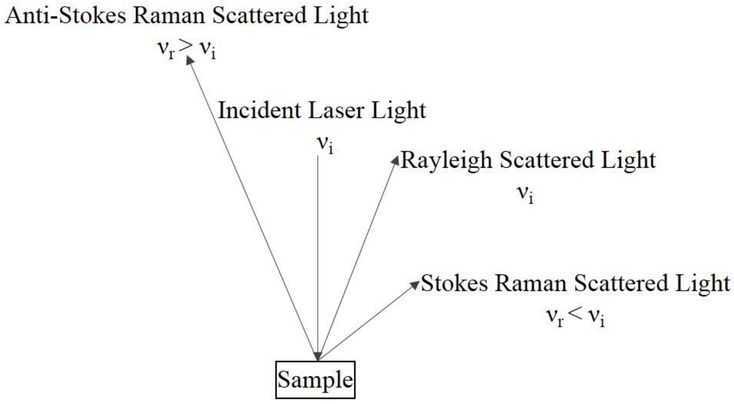

Figure 6 - Schematic sketch of some scattering processes when a laser beam hits a sample surface. Rayleigh scattering and Raman scattering processes. After reference [17].

In this work a Raman Spectrometer, model XY-800 from Dilor, was used. In Figure 7 its measurement system is presented [18]. It is a triple grating spectrometer that is connected to an Ar^+/Kr^+ laser. For this work a green laser with the wavelength of 514 nm and the beam power of 40 mW were applied. The green laser beam is produced and emitted from the laser source. Before the beam interacts with the sample, it is directed by a mirror (M) to pass through a microscope objective with the magnification of 40x which results in a laser beam diameter of 10 µm. The scattered light is then directed back by the mirror and collected by a collecting lens (C) to pass the beam through the first split, which is in the first stage, and then further towards the first spherical mirror (S M). The spectral resolution is depending on the widths of the slits openings, which was set to 200 µm. The first and second stage contains two parallel rotating gratings (G) that will reject the Rayleigh scattering, which results in that only Raman Scattering is remained [19]. In the final stage, the Raman Scattering is directed towards a charge-coupled device (CCD) camera.

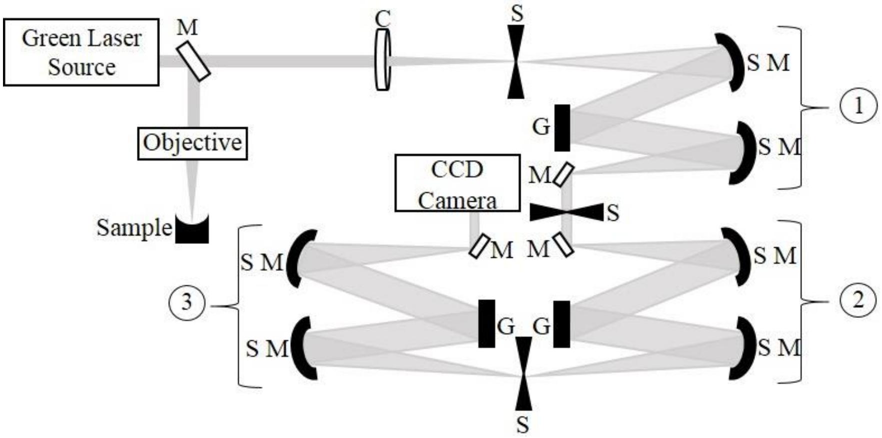

Figure 7 - Schematic illustration of a Raman Spectrometer, Dilor XY-800, used in this study. After reference [18].

Some factors that needs to be kept in mind while analysing the obtained data are for example the penetration depth of the laser beam while it hits the sample. When a very thin oxide film on a metal substrate is measured, the Raman spectrum signal may come from mainly the metal substrate. Another factor could be the mounting of the sample, since the surfaces are curved, the beam needs to be directed in the middle of the sample to be able to detect the scattered light right above since that is where the detector is.

5.3 SCANNING ELECTRON MICROSCOPY

When the interest is to view the structure of a sample surface, Scanning Electron Microscopy (SEM) is often chosen [20]. A scanning electron microscope can provide surface morphology information in a size from micrometre to nanometre. In this thesis work is the SEM model Ultra 55 from LEO used. Some key operating parameters to be able to acquire high resolution micrographs has been for example acceleration voltage 5 kV, a working distance of 3 mm and using an inlens detector.

In Figure 8 the main parts of a SEM instrument is illustrated. The high-energy electrons in the beam, called primary electrons, are generated in an electron source and then entering a vacuum chamber [21]. The condensing lenses will focus the beam and the apertures excludes the electrons with too high angle. The scanning coils causes the beam to scan the surface in a grid and the objective lens will focus the electron beam onto the sample. An interaction between the primary electrons and the atoms of the sample occurs within an interaction volume. This interaction produces different types of signals that can be detected with suitable detectors for respective signals. Some examples of these signals are backscattered electrons, secondary electrons and characteristic X-rays.

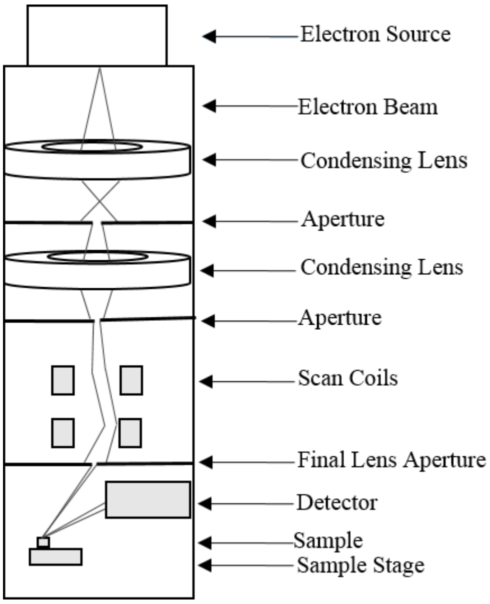

Figure 8 - Schematic illustration of a Scanning Electron Microscope instrument. After reference [20].

Figure 9 illustrates the interaction volume and different types of signals [22]. The backscattered electrons are produced when a primary electron hits a sample atom and an interaction occurs which causes the path of the electron to deviate from its original path and thus leaving the sample [20]. The secondary electrons are derived from when the primary electrons kicks out the electrons from the atoms of the sample. Characteristic X-rays are produced when tightly bonded sample electrons are ejected from the inner shell, this creates an electron hole which is filled with an electron from a higher energy shell [20]. The energy difference between the shell above and the shell below is released in the form of emitted characteristic X-rays.

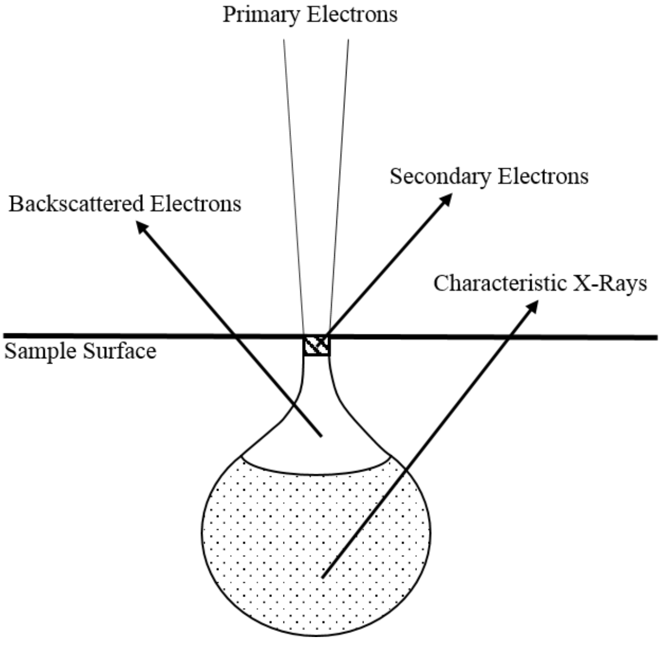

Figure 9 - Schematic illustration of the interaction between the electron beam and the sample. After reference [20].

5.3.1 ENERGY DISPERSIVE X-RAY SPECTROSCOPY

Energy Dispersive X-ray Spectroscopy (EDS) analysis in SEM is a method used to collect and convert the detected characteristic X-rays into elemental composition data [21]. Characteristic X-rays are emitted when tightly bonded electrons are ejected from an inner shell. These X-rays can be detected with an EDS detector and thus convert the detected signals to elemental composition data [23].

In this work a LEO Ultra 55 SEM equipped with an Oxford Inca EDX system has been used for EDS analyses. An acceleration voltage of 12 kV or lower was used. This was due to the desire to make the interaction volume into the metal substrate as small as possible to be able to receive most of the signal from the formed oxide film. The EDS detector on the SEM used has an optimal working distance at 8 mm. The aperture size was chosen to 30 μm and an inlens detector was used for image formation during EDS work. The analysis time was set to 120 seconds per site and the obtained data was analysed by using the software INCA.

5.3.2 FOCUSED ION BEAM

When the task is to obtain a crossection of an oxide film or to produce a TEM lamella, a Focused Ion Beam (FIB) system can be used. In this thesis work the FIB-SEM instrument Versa3D LoVac DualBeam from FEI has been used. A FIB system is similar to a scanning electron microscope, it also includes a vacuum chamber but uses an ion beam instead of an electron beam to scan the sample [24]. This is a destructive technique since the purpose is to remove material from the sample to create a crossection. The liquid metal ion source produce an ion beam with the diameter of approximately 5 nm.

Figure 10a) shows a schematic drawing of a focused ion beam system, where a Gallium ion source produces the ion beam, a column where the ion beam is focused towards the sample which is placed on a samples stage. A FIB system can be incorporated in an SEM, where the ion beam is used to perform the milling while the image of the sample is obtained using the electron beam. A simplified sketch of the ion milling process is illustrated in Figure 10b) where the gallium ion is interacting with the sample surface, thus resulting in ions or electrons being sputtered away from the sample surface.

During the process of preparing a TEM lamella, which is a very thin sample slice, a platinum layer can be deposited on the area where the TEM lamella will be prepared, in the sense of protecting the oxide film. The platinum precursor that is used, involves for example carbon. First a platinum layer is deposited using the electron beam, which is a gentle deposition of platinum in contact with the oxide. A second platinum layer is then deposited using the ion beam.

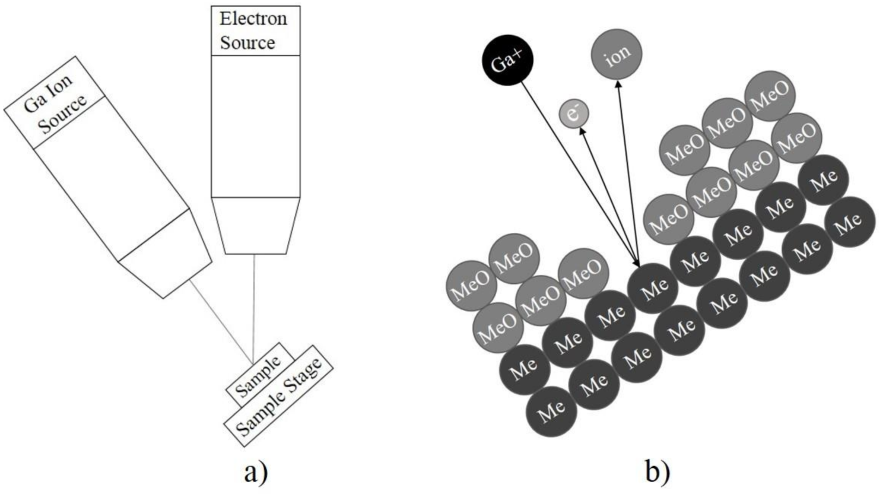

Figure 10 - Schematic drawing of (a) focused ion beam system and (b) ion milling process. After reference [25].

Some key operating parameters that have been used are the working distance of 10 mm and the sample was tilted 52° from the electron beam, since this results in 0° towards the ion beam. Before the milling process started, platinum was deposited on the area of interest to protect the oxide features.

5.4 TRANSMISSION ELECTRON MICROSOPY

Transmission Electron Microscopy (TEM) is a powerful analytical technique when analysing for example an oxide film since it is possible to obtain a resolution below 1 nm. TEM can accurately reveal the microstructure of an oxide film. Figure 11a) shows a sketch of a TEM, where an electron beam is directed towards a thin sample slice that should be thinner than 100 nm [25]. The TEM sample can be prepared by using a FIB system. As seen in Figure 11a), the electrons pass through the sample and are then detected. By performing an energy-dispersive x-ray analysis in TEM, an accurate chemical analysis with a spatial resolution in the range of nanometres can be obtained. The depth resolution depends on how thin a sample that has been prepared [23]. Figure 11b) illustrates a simplified sketch of the interaction between the electrons passing through a thin sample. The transmitted electrons will either be inelastically scattered, elastically scattered or remain unscattered, thus different information can be obtained.

The TEM instrument used in this work was a Titan 80-300 from FEI where one key operating parameter was the acceleration voltage of 300 kV.

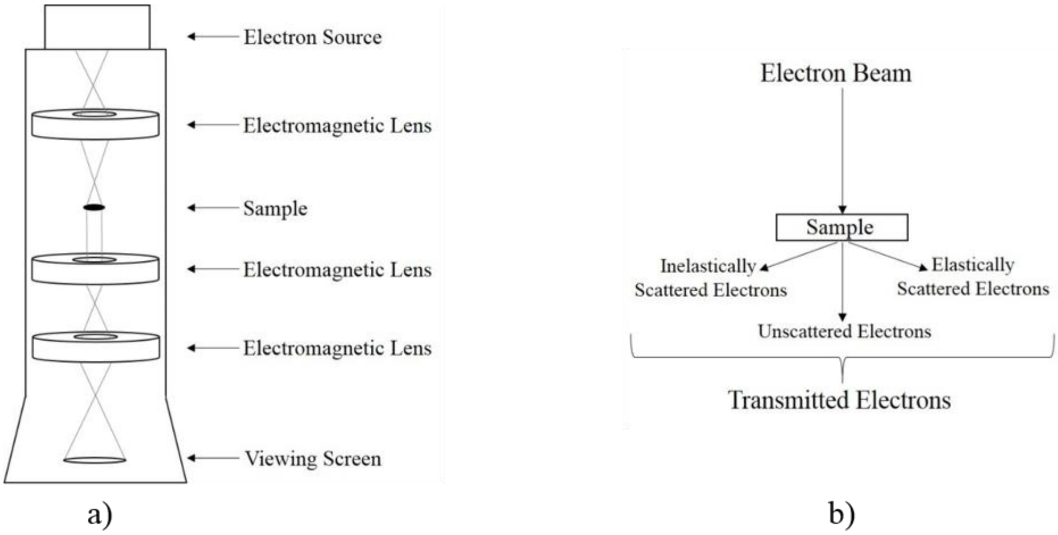

Figure 11 - Schematic drawing of (a) Transmission Electron Microscope instrument and (b) a simplified sketch of the interaction between the electron beam and the very thin sample. After reference [25].

5.4.1 ANALYTICAL TRANSMISSION ELECTRON MICROSCOPY

Since one task of this study is to detect where zinc is present in the formed oxide film, TEM equipped with EDS has been used. One of many advantages with TEM/EDS compared to SEM/EDS is the reduced interaction volume since a very thin sample is used in TEM instead of receiving signal from the metal substrate, which is the case for SEM/EDS.

The EDS measurements was performed on samples A1 and A3 on some areas of interest, which is the thin continuous oxide film, the crater oxide, the precipitated oxide grains and the spherical particles as an attempt to detect zinc. The EDS analyses were performed using an Oxford X-sight EDS detector and the analyses were carried out using the software TIA. To collect the data, area scans and point analyses were performed on the area of interest.

6. STUDIED MATERIALS AND TEST RIG FOR EXPOSURE

6.1 STUDIED MATERIAL

The elemental composition in weight percent of the main components in stainless steel 304L, which is the studied material in this thesis work, is summarized in Table 1. Regarding the tube, it had a non-polished inner surface, an outer diameter of 25 mm, a wall thickness of 4 mm and thus an inner diameter of 17 mm [26].

Table 1 - Elemental composition in weight percent of the studied material stainless steel 304L. After reference [12].

Material	Elemental Composition (wt-%)							
	S	C	P	Si	Mn	Ni	Cr	Fe
Stainless Steel 304L	0.012	0.013	0.030	0.47	1.65	10.5	18.72	Bal.

6.2 SIMULATED PWR HOT LEG ENVIRONMENT

The exposure environment was designed to simulate exposure of PWR steam generator material, SS 304L, for the hot leg as similar as possible to the operating mode of a PWR at Ringhals. In the circuit before the main flow enters the sample tube legs, the cold wetted surface was of SS316 and the hot wetted surface was of either Ziraloy-4 or Alloy 690 [26]. The exposure parameters are summarized in Table 2.

Table 2 - Exposure parameters that have been used during the exposure. After reference [26].

Exposure Parameter	Value
Temperature [°C]	325
pH_{300}	7.4
B [ppm]	700
Li [ppm]	4.12
H_2 [ppb]	4000
H_2 [ml/kg H_2O]$_{STP}$	45
Co-60 [Bq/kg]	200
Total Co [ppb]	0.009
Flow rate [kg/h]	6
Zn-dosage [ppb]	0; 5; 10

Zinc in the form of zinc acetate was used. The total flow rate of the entering main flow was 6 kg/h, which then was divided into separate sample tube legs resulting in 3 kg/h, thus the flow velocity in each sample tube leg was 0.5 cm/s [26]. By injecting zinc at different time intervals, the effect of zinc on the uptake of radioactive Co-60 in the SS 304L could be studied in detail. Another effect of zinc could also be studied, which was the possibility of zinc to remove already incorporated radioactive Co-60 in the SS 304L by stopping the addition of radioactive Co-60 for a period of time. The addition of zinc was either 5 ppb or 10 ppb. The measured radioactivity uptake of samples A1, A3 and B1 are shown in Figure 12 a) and b). When zinc was added it could be observed that the rate of the radioactivity uptake partly levelled out. When no radioactive cobalt was added, it could also be observed that the amount of already incorporated Co-60 decreased.

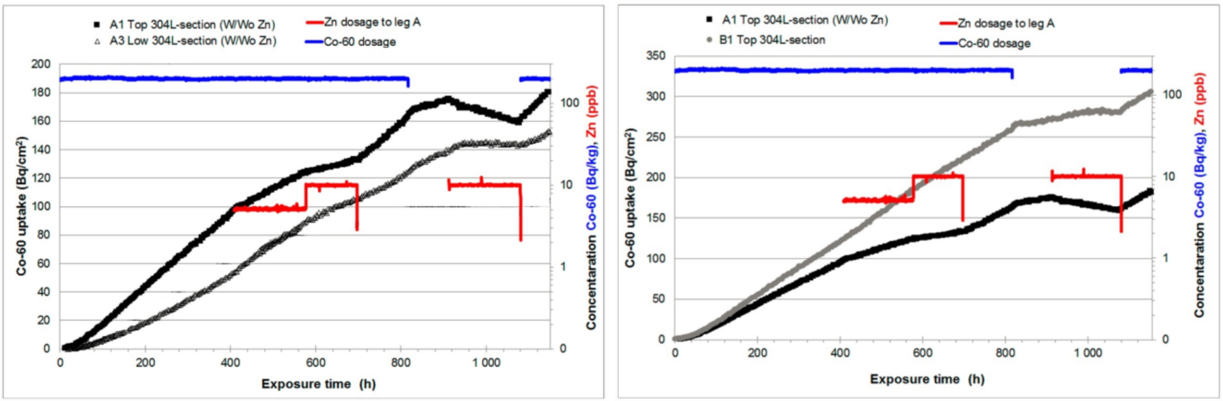

a) b)

Figure 12 - (a) Measured radioactivity uptake of Co-60 on sample A1 and A3 when zinc is added. (b) Measured radioactivity uptake of Co-60 on sample A1 and B1, where zinc is added for sample A1. After reference [12].

6.3 TEST RIG FOR AUTOCLAVE EXPOSURE

An illustration of the test rig is shown in Figure 13. The exposure parameters are summarized in Table 2 and the exposure process of the samples in the test rig are explained as follow [26].

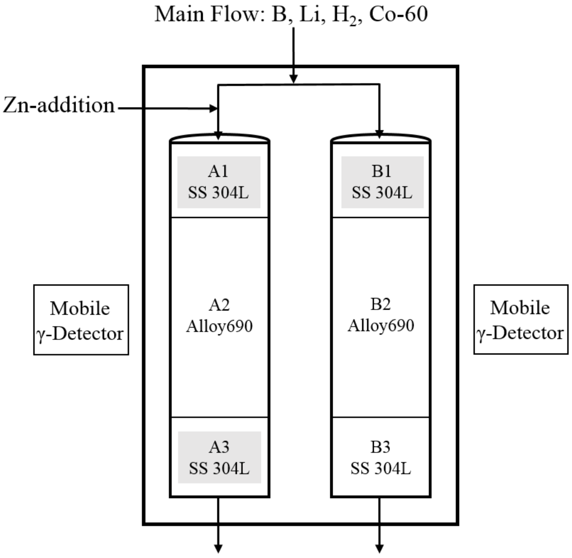

Figure 13 - Simplified sketch of the test rig. After reference [26].

As can be seen in Figure 13, the different pipes have been mounted in the test rig before the exposure started. The main flow entered the test rig from the top and was divided into two parallel sample tube legs, leg A and leg B.

To be able to expose the samples at the right temperature, an oven of convection type was used, which is illustrated by the vertical bold rectangle surrounding leg A and leg B in Figure 13 [26]. Measurements of the activity uptake on leg A and leg B were performed using two mobile gamma detectors that scanned each leg. After the flow passed through the oven, the outlet water chemistry was analysed by using integrated filters and collecting water samples. This was performed with the purpose of revealing information regarding the activity and the amount of corrosion products in the outlet.

After the exposure was finished, the tube legs were dismantled and samples were cut out from the legs. The edges of the samples were smoothened by grinding with SiC paper, ultrasonic cleaned in ethanol and acetone and then dried. The samples were then stored in separate plastic bags until they were silver-glued onto metal stubs for further analysis.

7. RESULTS AND DISCUSSIONS

7.1 XRD

In this work, the corroded surfaces of A1, A3 and B1 samples have been subjected to XRD measurements. For the sake of easy comparison, a freshly polished test coupon of type 304L has also been measured. In Figure 14, Figure 15, Figure 16 and Figure 17, the XRD patterns for the unexposed, A1, A3 and B1 samples are shown, respectively. In each figure the peaks are matched with the Powder Diffraction File (PDF) database. The black filled squares illustrate peaks originated from the metal SS 304 and the hollow squares mark other unidentified metal substrate peaks. By comparing the diffractograms, one can see that, on the surfaces of A1, A3 and B1 samples, there are additional diffraction peaks that are absent in the XRD pattern of the metal substrate. All peaks from nickel ferrite, illustrated with black triangles, can be found in the measured XRD pattern, which indicates the presence of spinel phase on all sample surfaces. However, there are a few diffraction peaks that have not been positively identified, illustrated with question marks. The d-values and the intensities of diffraction peaks obtained for each sample are also listed in Table 3, where question marks are used for unidentified peaks. PDF files for some plausible phases from PDF are presented in Table 4.

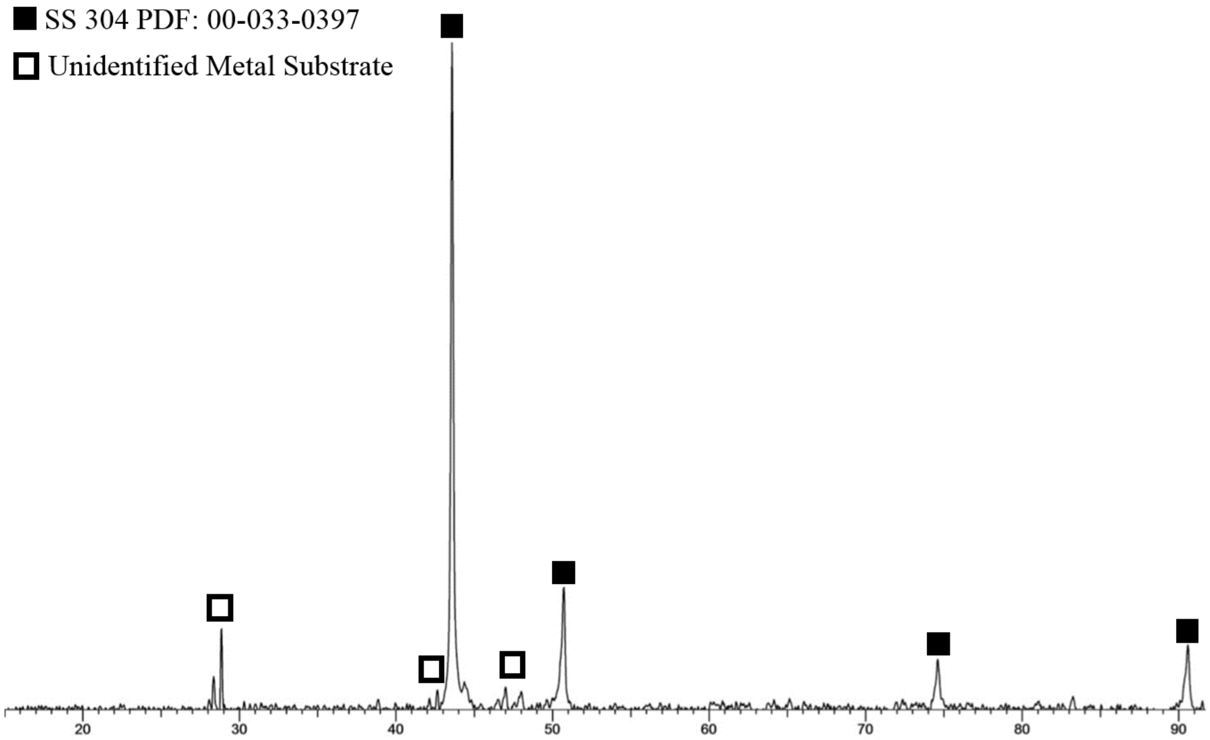

Figure 14 - Fresh unexposed reference sample.

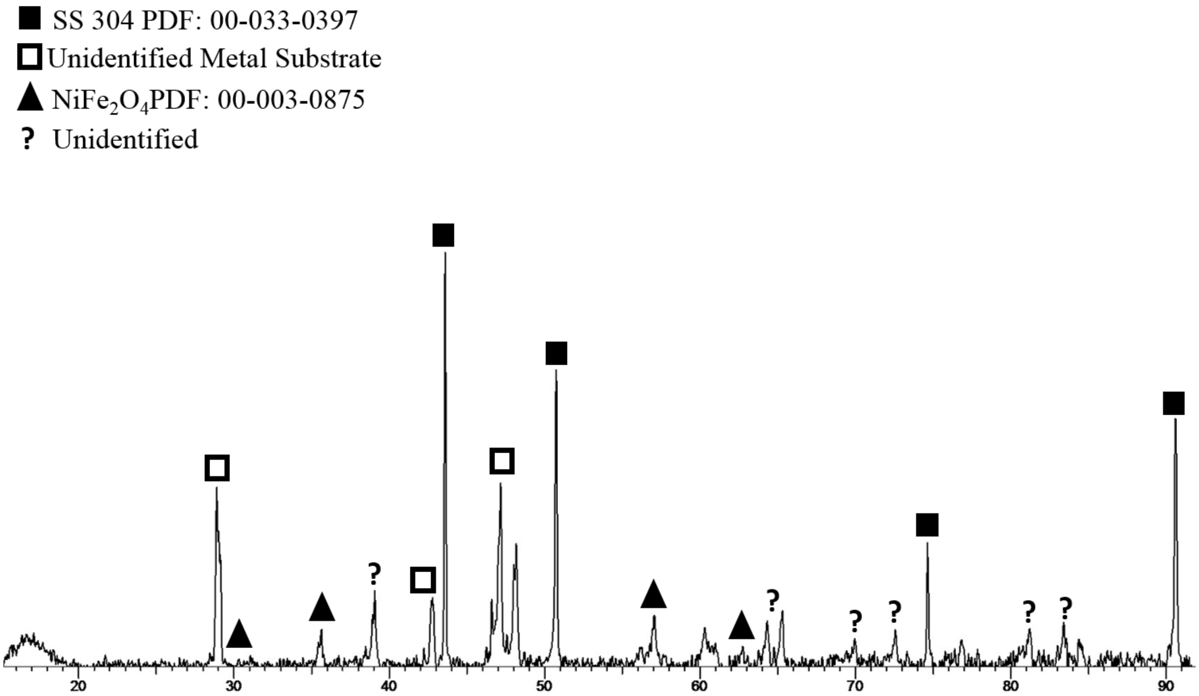

Figure 15 - XRD pattern for sample A1.

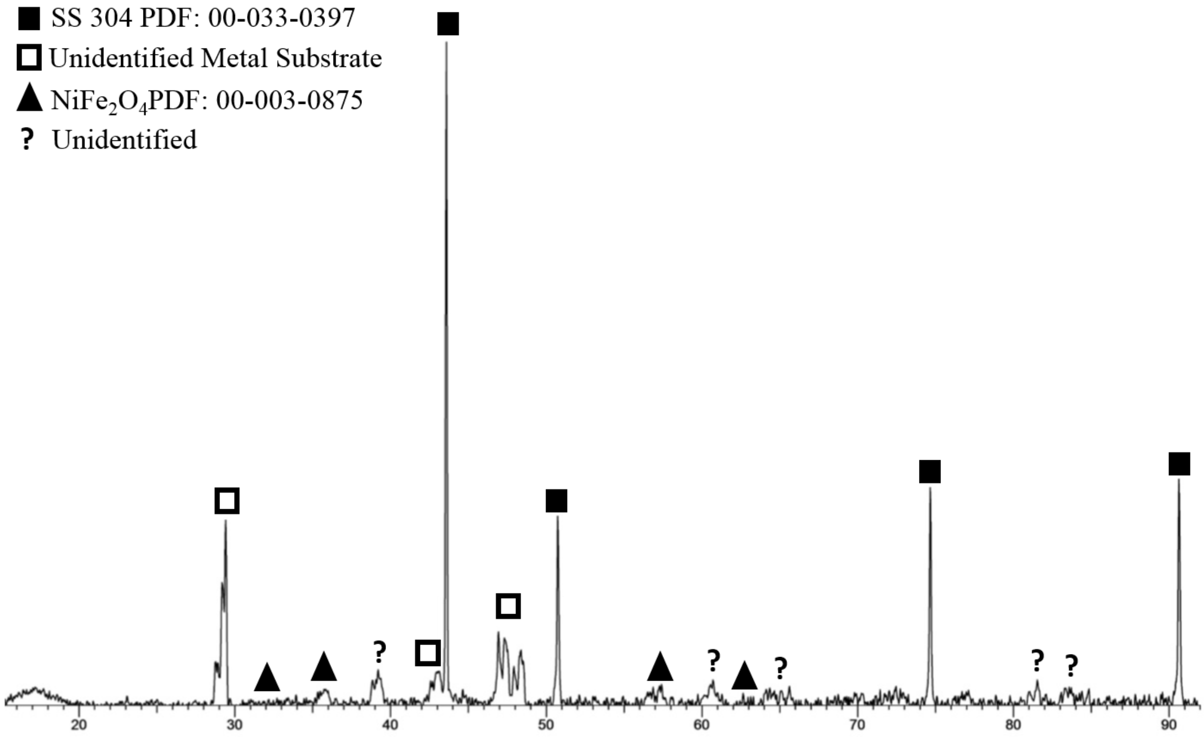

Figure 16 - XRD pattern for sample A3.

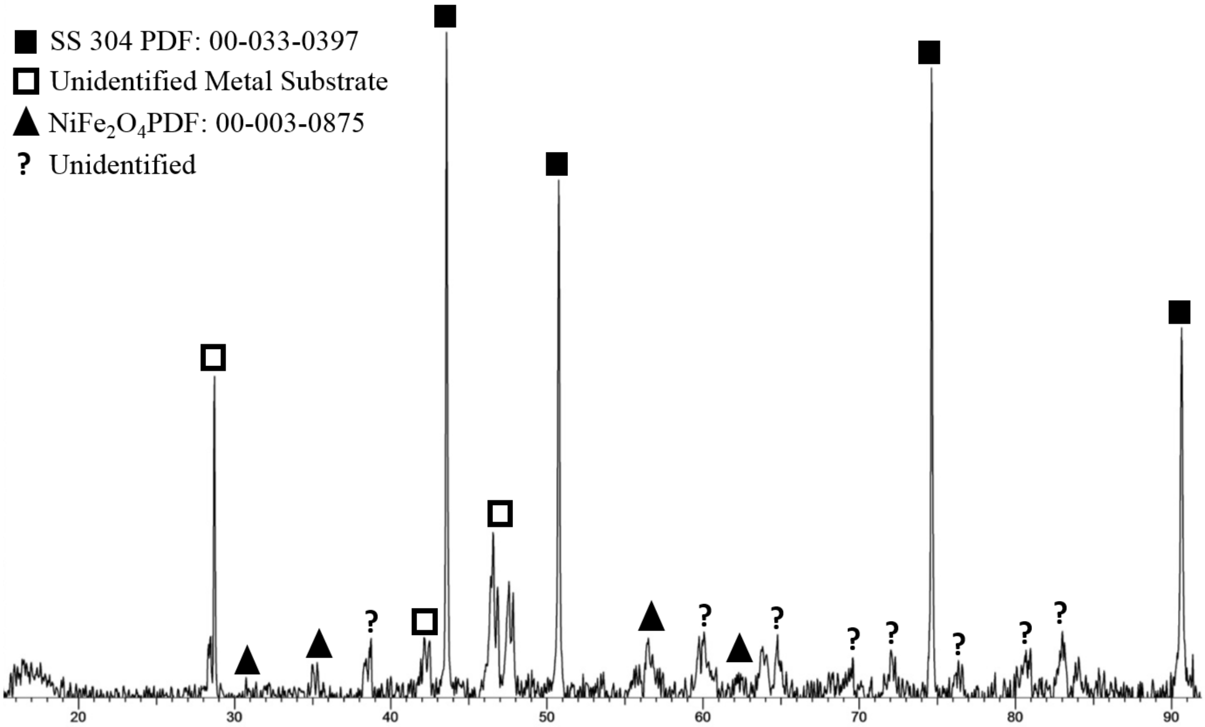

Figure 17 - XRD pattern for sample B1.

The encountered challenges during the XRD measurements were for example to find the right position on the sample surface, which was in the middle of the sample. The incident x-rays were intended to be directed towards the middle of the sample in such an orientation that the diffracted x-rays would be collected from the same area of identical height and not from an area of different heights. Another factor that needed to be considered was to find the right height of the sample that was mounted in the sample holder by being pressed down into modelling clay. The reason for wanting to achieve the right height of the sample was to avoid measuring from the edge of the samples since it had a curved surface.

Table 3 - XRD data obtained for A1, A3 and B1 samples and the metal substrate. The peaks marked with a question mark, are peaks that are challenging to distinguish from the background noise.

Metal Substrate		A1		A3		B1	
d [Å]	I_{Rel} [%]	d [Å]	I_{Rel} [%]	d [Å]	I_{Rel} [%]	d [Å]	$I_{Re.l}$ [%]
3.09	18.7	3.09	43.2	3.04	27.3	3.10	48.7
		2.512	8.9	2.51	2.3 (?)	2.51	4.9 (?)
		2.31	18.4	2.39	4.9 (?)	2.32	7.7 (?)
2.11	3.0	2.11	14.8	2.10	5.0 (?)	2.14	8.5 (?)
2.07	100.0	2.08	100.0	2.08	100.0	2.08	100.0
1.93	4.0	1.93	44.6	1.93	10.9	1.94	24.8
1.89	3.1	1.89	29.8	1.88	8.1	1.90	17.3
1.79	17.9	1.80	69.7	1.79	27.9	1.79	78.5
		1.64	4.6 (?)			1.64	6.1 (?)
		1.61	12.5	1.62	1.8 (?)	1.62	8.9
				1.61	1.9 (?)		
		1.53	9.5	1.53	2.8 (?)	1.53	8.9
		1.48	4.7 (?)	1.48	1.7 (?)	1.48	3.0 (?)
		1.45	11.0	1.45	1.0 (?)	1.45	7.4 (?)
		1.43	13.6	1.42	2.5 (?)	1.43	9.4
		1.34	6.7 (?)			1.34	4.4 (?)
		1.30	8.9			1.30	6.1 (?)
1.27	7.7	1.27	30.1	1.27	32.6	1.27	95.2
		1.18	9.2	1.18	0.7 (?)	1.18	5.0 (?)
		1.16	10.7	1.15	2.3 (?)	1.16	9.9
		1.15	6.5 (?)	1.14	1.8 (?)	1.15	5.9 (?)
1.08	9.8	1.08	60.4	1.08	32.3	1.083	56.1

Table 4 - Plausible phases from the PDF.

PDF 00-033-0397: SS 304		PDF 00-003-0875: $NiFe_2O_4$	
d [Å]	I_{Rel} [%]	d [Å]	I_{Rel} [%]
2.075	100	2.950	20
1.796	45	2.510	100
1.270	26	1.600	33
1.083	30	1.480	53

7.2 LRS

Figure 18 to Figure 20 show the Raman spectra obtained for the corroded surfaces of samples A1, A3 and B1. The spectra obtained for samples A1 and B1 lack details while the spectrum for sample A3 sample has many more Raman peaks, although there was no detectable difference between the three samples in their XRD patterns.

By comparison with a spinel oxide reference of nickel ferrite, $NiFe_2O_4$ in Figure 21, from a previous work by Graves et al. [27], all peaks in the Raman spectrum for A3 sample have similar positions as the spinel phase, which are at 338 cm^{-1}, 491 cm^{-1}, 569 cm^{-1} and 702 cm^{-1}. A possible explanation for this is that, although the measurements were done under similar instrumental conditions, the better signals as detected on A3 sample than on A1 and B1 samples could be associated with the uneven surfaces and difficulty for a perfect mount on the sample stage. Due to the limited time allowed for this work, no further effort has been made to repeat the measurement by optimizing the conditions.

From literature data [28] one can see that different spinel phases have rather similar Raman spectra. Therefore, if there is more than one spinel phase in the oxide films, they may not be easily distinguishable.

Another factor that needs to be considered is the penetration depth of the laser beam into the sample, which could be a few micrometres for an ordinary bulk oxide sample. Since the oxide films studied in this work are very thin, based on the literature [28], most of the noise signals would have been due to the metal substrate, and the Raman peaks from the thin oxide films are expected to be weak.

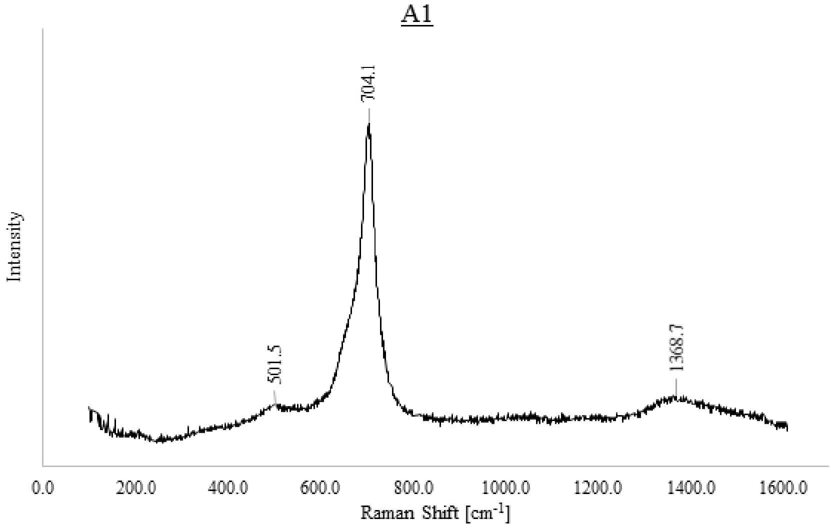

Figure 18 - Raman spectrum for sample A1.

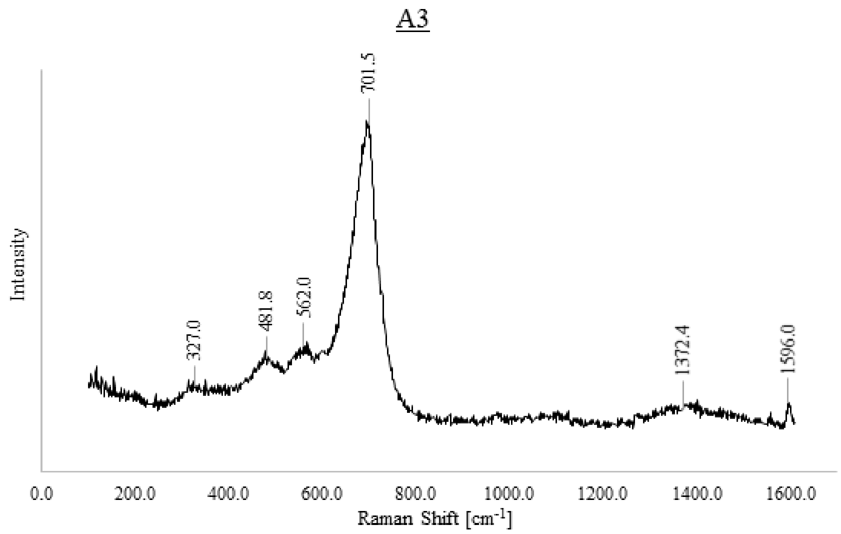

Figure 19 - Raman spectrum for sample A3.

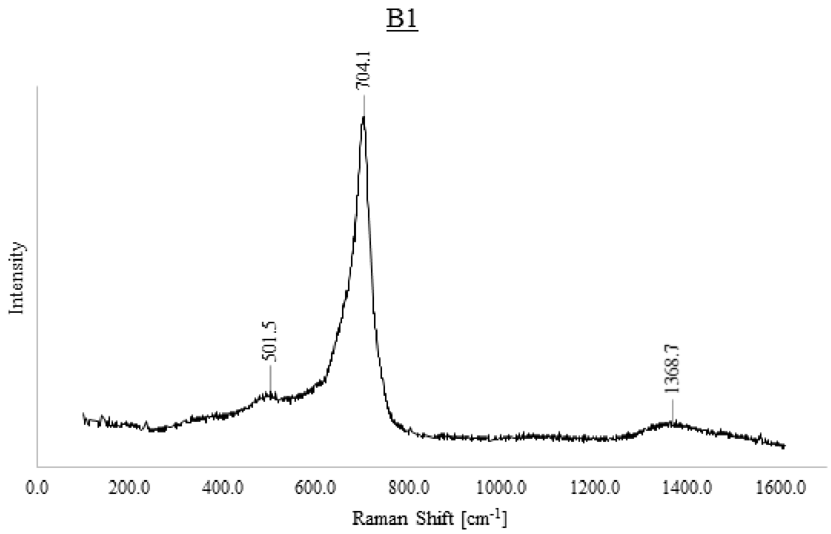

Figure 20 - Raman spectrum for sample B1.

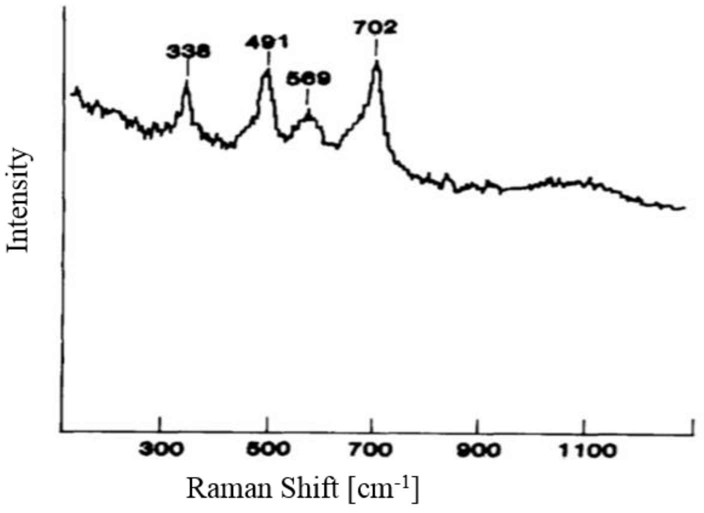

Figure 21 - Raman spectrum for nickel ferrite [27].

7.3 SEM

Figure 22, Figure 24 and Figure 26 are overview SEM Secondary Electrons (SE) images from the corroded surfaces of samples A1, A3 and B1, respectively. Similar images but at a higher magnification are presented in Figure 23, Figure 25 and Figure 27. One can see on all corroded surfaces that there are grains with two kinds of characteristic shapes. One has a relative large grain size (~100-200 nm) and sharp edges. Another has spherical shape but with a much smaller size (~30 nm). Note that the relative abundance of the spherical grains as seen in Figure 23 and Figure 25 is somewhat exaggerated. Figure 27 is in fact a more representative image for all samples at the specific magnification. In other words, these spherical grains appeared only in some locations in form of agglomerates on each sample surface.

Due to the lack of time the actual abundance of each kind of surface grains has not been determined in this work. Based on visual inspection one cannot get an impression of any difference in grain abundance (amount of grains formed) between the three different samples.

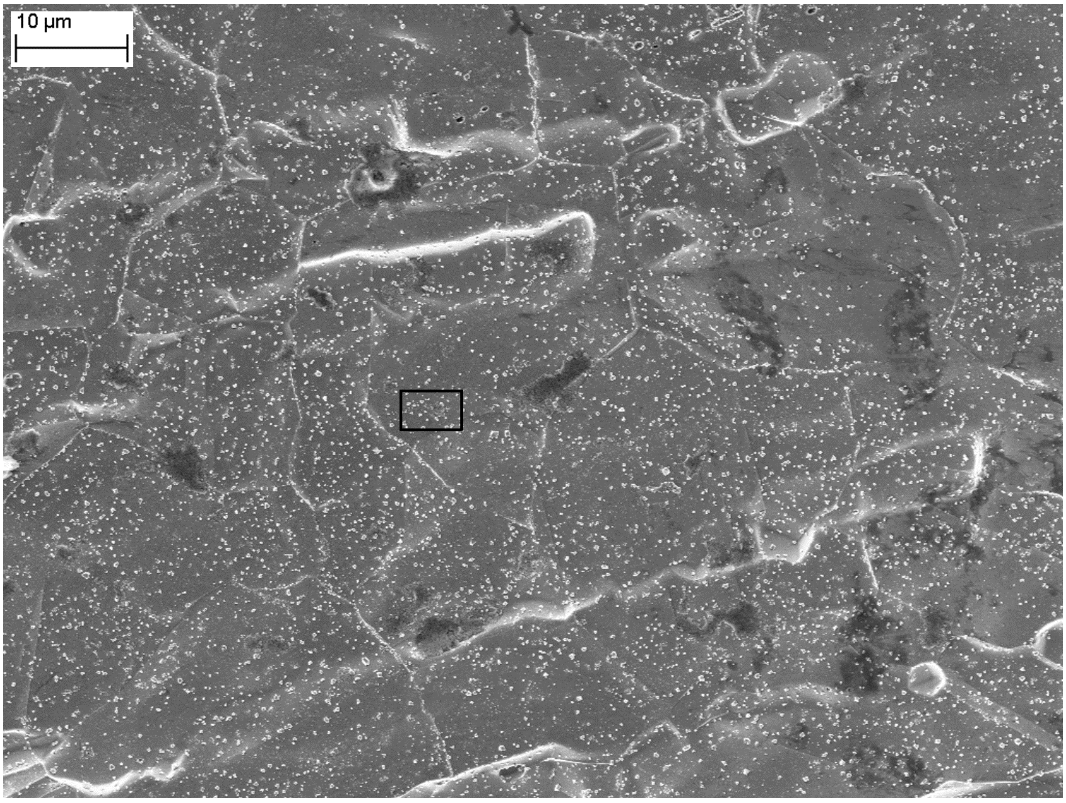

Figure 22 - SEM SE image for sample A1 showing an overview of a representative area. The marked area is observed at higher magnification in Figure 23.

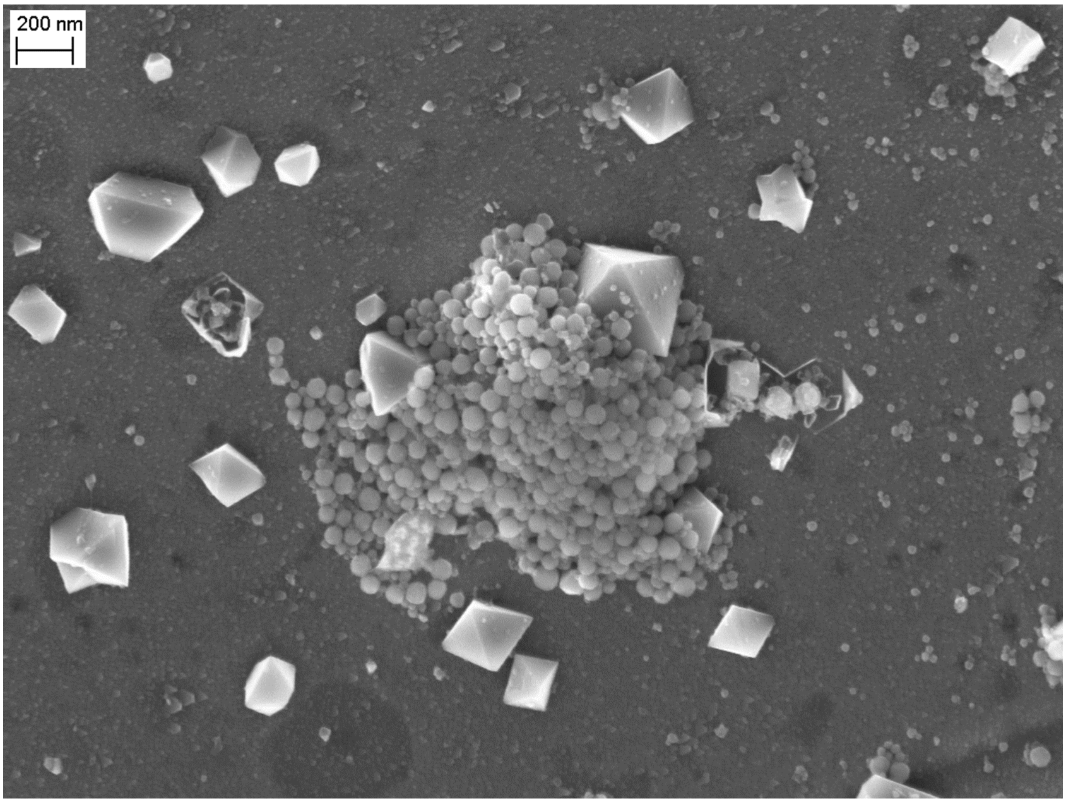

Figure 23 - SEM SE image showing an area marked in Figure 22 from sample A1. Precipitated oxide crystals and spherical particles can be observed.

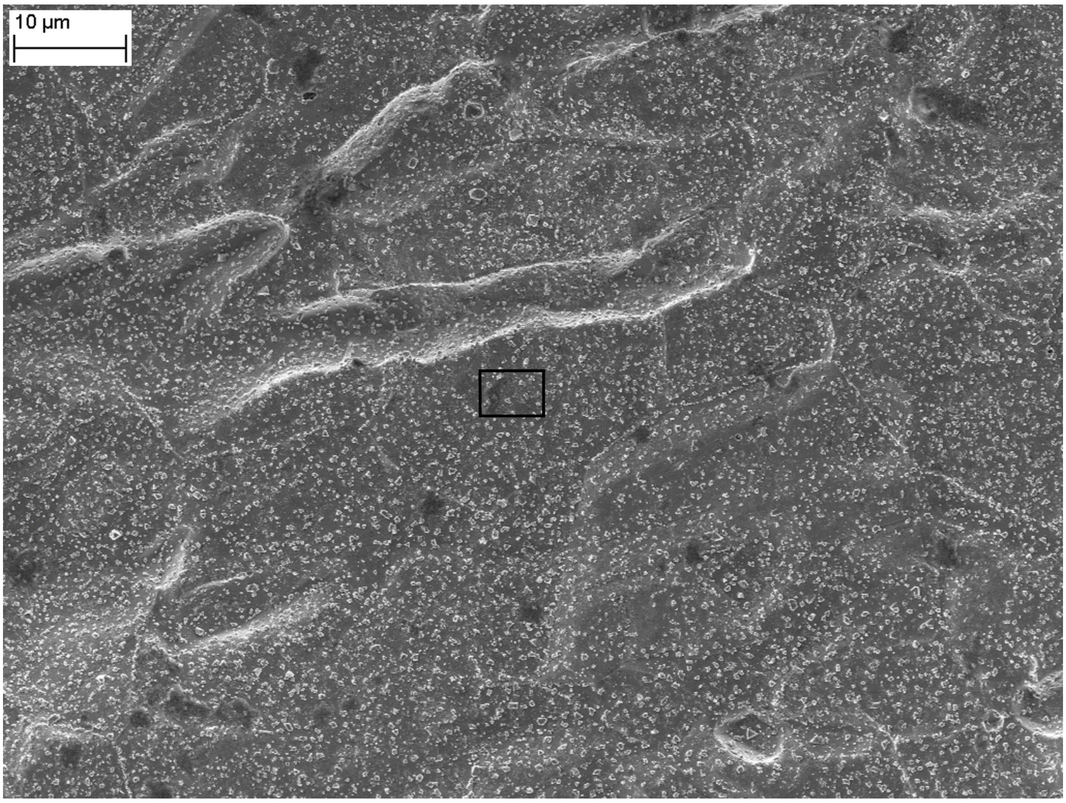

Figure 24 - SEM SE image for sample A3 showing an overview of a representative area. On the rough metal grain boundaries, relatively large grains and agglomerates of spherical particles (very dark area) can be seen. The area inside the marker is shown in Figure 25 at a higher magnification.

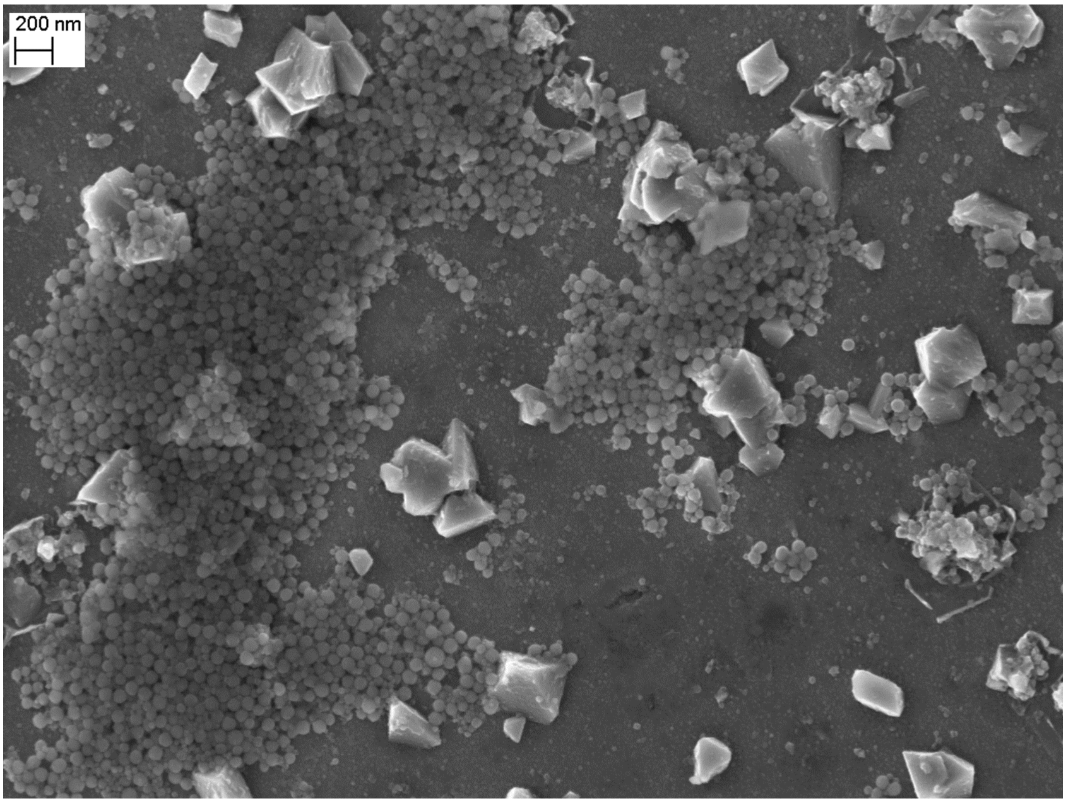

Figure 25 - SEM SE image showing an area marked in Figure 24 from sample A3. Well-structured oxide crystals and spherical particles can be observed.

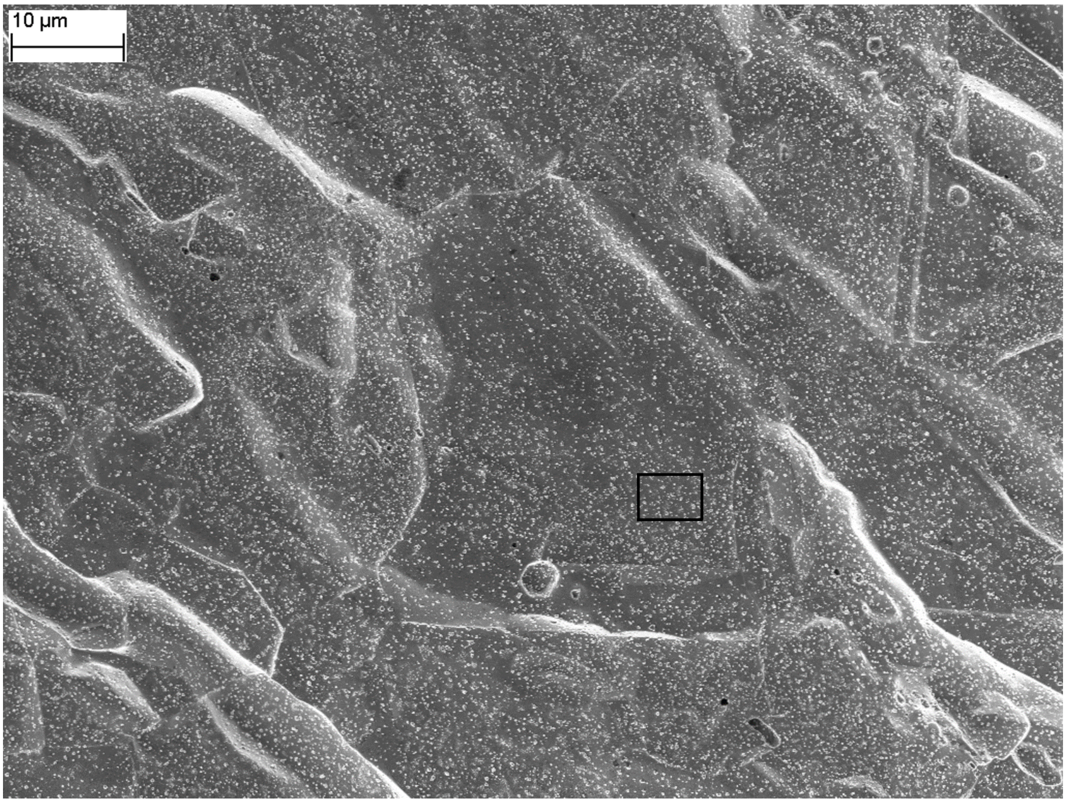

Figure 26 - SEM SE image for sample B1 showing an overview of a representative area. The marked area is observed at a higher magnification in Figure 27.

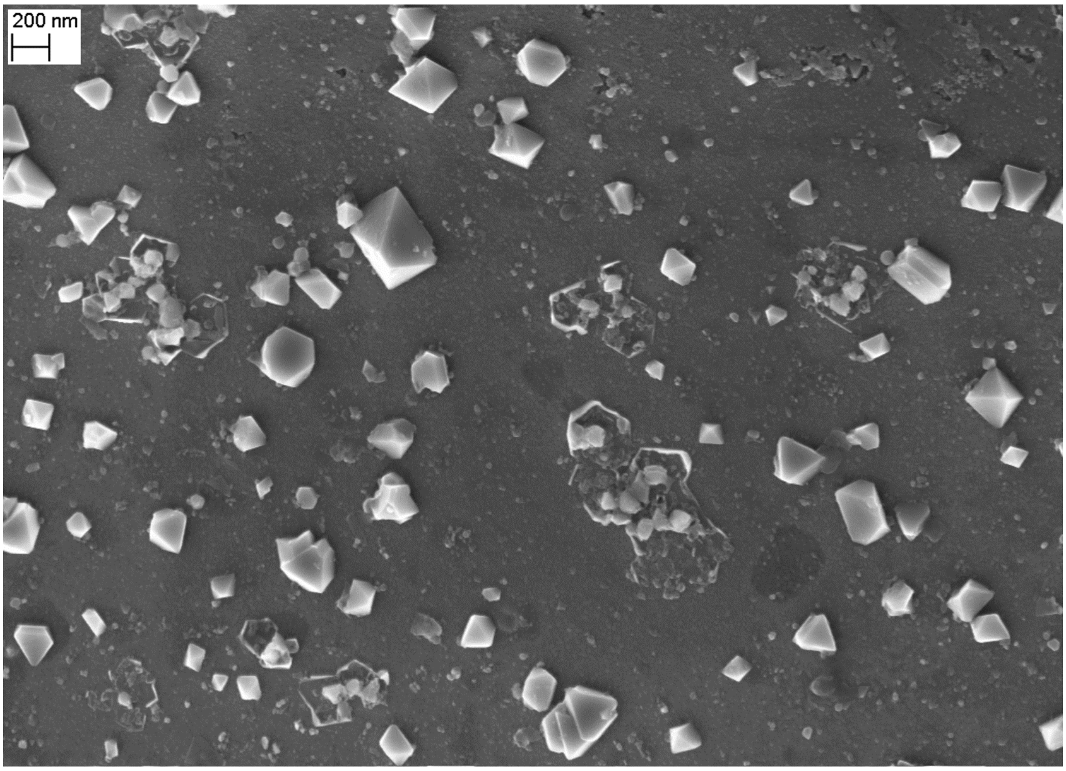

Figure 27 - SEM SE image showing an area marked in Figure 26 from sample B1. This area is deemed to be representative for all sample surfaces (A1, A3 and B1), where much fewer spherical particles can be seen.

7.3.1 SEM/EDS

Elemental compositions of some selected surface grains and areas on samples A1, A3 and B1 have been determined with EDS in SEM at 12 kV. See Figure 28 - Figure 30 for A1, A3 and B1 respectively. The results of the analyses are summarised in Table 5 to Table 7. In the tables, a tentative formula for the suspected spinel phase of AB_2O_4 type (A=Me^{2+} and B=Me^{3+}) is also presented for each grain/location measured by normalising the compositions for Ni, Cr and Fe to 100 at-%. Recall that at 12 kV the penetration depth of the electron beam is approximately 0.5 µm, being similar to or slightly larger than the surface grain size, a fraction of the characteristic X-rays detected would have come from the regions underneath the surface grains. This is evident when relatively low oxygen contents (compared to 57 at-% oxygen content in a spinel phase) were detected at *e.g.* the sites 5 and 6. The relatively high oxygen contents measured at the sites 1-4 (Sample A1) might suggest that the beam-matter interaction volume consisted mainly of oxide films. At the site 3 (Sample A1), the darker area with the spherical particles present, approximately 6 at-% of silicon was also detected. The analyses on these two types of the surface grains in sample A1 have been further examined in TEM and will be presented in Chapter 7.4.

If the measured points having the highest oxygen content in each sample are compared and assume that the interaction volume (Sample A1) was solely spinel (the red marked lines in the tables), one can see that the presumed spinel in sample A1 contains slightly lower Cr content than in sample A3, or than in sample B1. Accordingly, the presumed spinel in sample A1 contains slightly higher Ni content than in sample A3, or than in sample B1. The Fe contents in the presumed spinels in all three samples are similar.

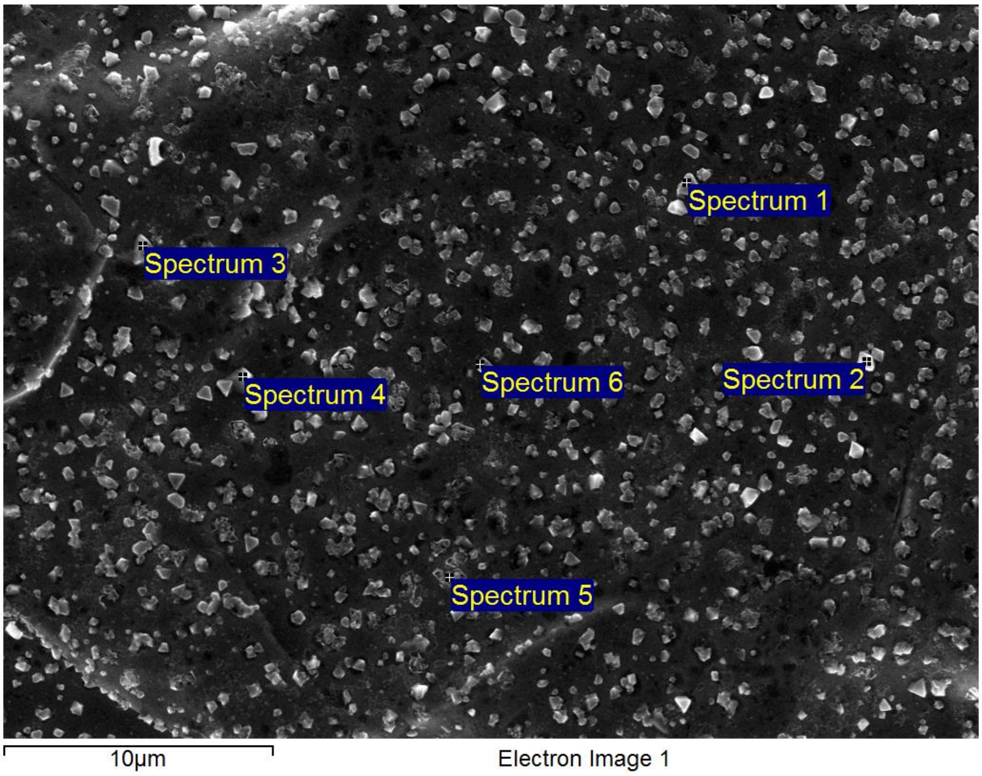

Figure 28 - SEM SE image showing EDS measurement positions on sample A1.

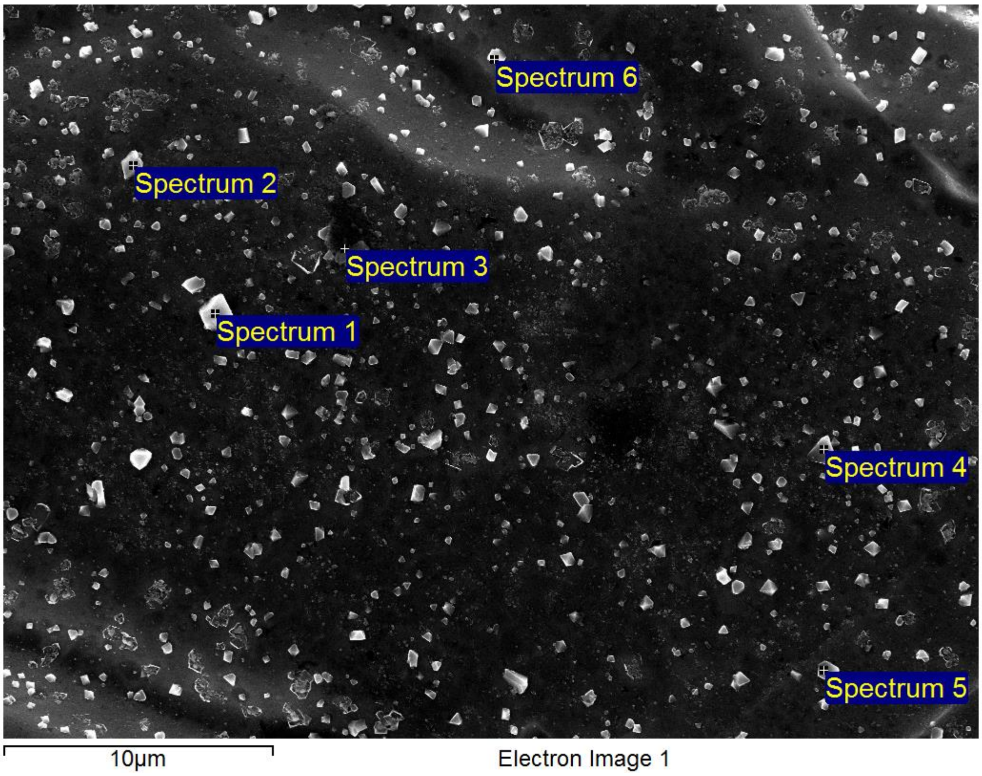

Figure 29 - SEM SE image showing EDS measurement positions on sample A3.

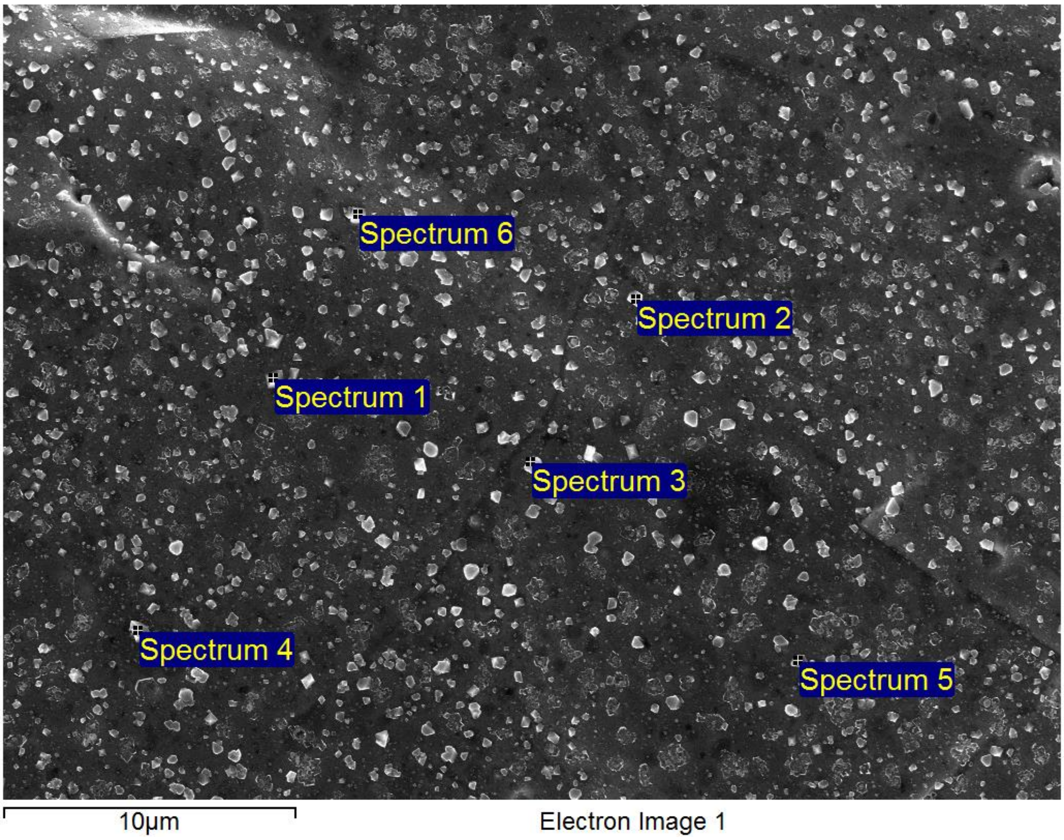

Figure 30 - SEM SE image showing EDS measurement positions on sample B1.

Table 5 - Elemental compositions of some measured surface grains/locations on sample A1 surface.

Site	C	O	Al	Si	Cr	Mn	Fe	Ni	$Ni_xCr_yFe_zO_4$
1	**2.98**	**49.95**			**3.47**	**0.47**	**33.45**	**9.67**	**$Ni_{0.62}Cr_{0.22}Fe_{2.15}O_4$**
2	3.57	43.17	1.07	0.63	6.99	1.58	36.11	6.87	$Ni_{0.41}Cr_{0.42}Fe_{2.17}O_4$
3	5.05	42.95	1.50	6.21	9.35	0.76	26.32	7.86	$Ni_{0.54}Cr_{0.64}Fe_{1.81}O_4$
4	2.27	42.59		0.47	10.49	0.78	36.00	7.39	$Ni_{0.41}Cr_{0.58}Fe_{2.00}O_4$
5		36.01		0.83	19.37	1.30	34.73	7.76	$Ni_{0.38}Cr_{0.94}Fe_{1.68}O_4$
6		25.32		0.67	31.49	2.00	34.13	6.39	$Ni_{0.27}Cr_{1.31}Fe_{1.42}O_4$

Table 6 - Elemental compositions of some measured surface grains/locations on sample A3 surface.

Site	C	O	Al	Si	Cr	Mn	Fe	Ni	$Ni_xCr_yFe_zO_4$
1	3.89	32.74	0.39	0.44	7.16	0.80	44.76	9.82	$Ni_{0.48}Cr_{0.35}Fe_{2.17}O_4$
2	3.27	34.69	0.54		10.24		43.95	7.31	$Ni_{0.36}Cr_{0.50}Fe_{2.14}O_4$
3	3.57	22.02		3.47	13.15	0.91	47.09	9.79	$Ni_{0.42}Cr_{0.56}Fe_{2.02}O_4$
4	**2.33**	**40.10**		**0.52**	**9.45**	**0.72**	**36.53**	**10.35**	**$Ni_{0.55}Cr_{0.50}Fe_{1.95}O_4$**
5	3.05	11.63		0.78	18.06	1.21	53.33	11.94	$Ni_{0.43}Cr_{0.65}Fe_{1.92}O_4$
6	3.63	10.57		0.82	17.50	1.05	54.42	12.02	$Ni_{0.43}Cr_{0.63}Fe_{1.94}O_4$

Table 7 - Elemental compositions of some measured surface grains/locations on sample B1 surface.

	C	O	Al	Si	Cr	Mn	Fe	Ni	$Ni_xCr_yFe_zO_4$
1	2.82	36.28	0.41	0.27	7.79	1.06	43.84	7.53	$Ni_{0.38}Cr_{0.40}Fe_{2.22}O_4$
2		37.93	2.00		11.41	2.94	38.30	7.42	$Ni_{0.39}Cr_{0.60}Fe_{2.01}O_4$
3	2.80	33.57	1.27	0.37	9.13	2.00	42.13	8.74	$Ni_{0.44}Cr_{0.46}Fe_{2.11}O_4$
4		**56.04**			**5.50**	**0.69**	**30.48**	**7.30**	$\mathbf{Ni_{0.51}Cr_{0.38}Fe_{2.11}O_4}$
5	3.06	32.51	0.40	0.62	14.55	1.41	38.64	8.81	$Ni_{0.43}Cr_{0.70}Fe_{1.87}O_4$
6	2.77	38.21	0.38	0.58	14.71	1.19	35.57	6.59	$Ni_{0.35}Cr_{0.78}Fe_{1.88}O_4$

7.3.2 FIB/SEM

In Figure 31, a cross-section SEM SE image of the relatively large surface grain with sharp edges can be viewed. It was obtained by using FIB technique. Such grains have been examined in detail by TEM and the results are presented in the following chapter.

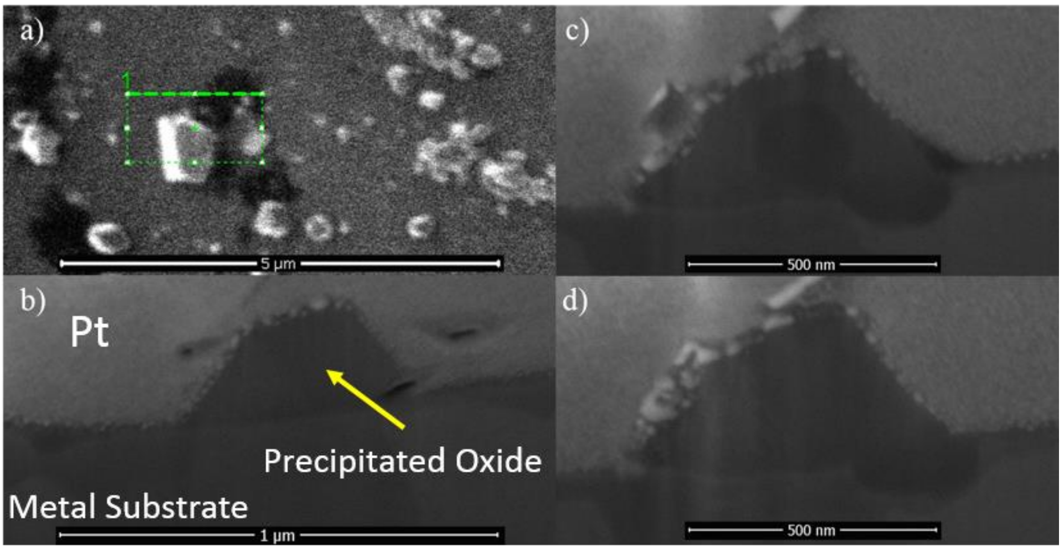

Figure 31 - SEM SE images showing a cross-section of a precipitated oxide.

7.4 TEM

7.4.1 Cross-section microstructures of sample A1

Figure 32 to Figure 35 show STEM (Scanning TEM) bright field (BF) and dark field (DF) images of a part of a cross-section TEM-lamella prepared from sample A1, in which the large precipitated oxide crystals, the small spherical particles, thin oxide film and crater oxides are indicated. HR TEM images in some areas of interest are presented in Figure 36 and Figure 37. Results from the elemental composition measurements are shown in Figure 38 to Figure 41 with corresponding data summarised in Table 8 to Table 10.

The thickness of the thin oxide film was measured at 15 random locations, (avoiding crater oxides and precipitated oxide crystal) and thus estimated to 15.9 ± 3.2 nm.

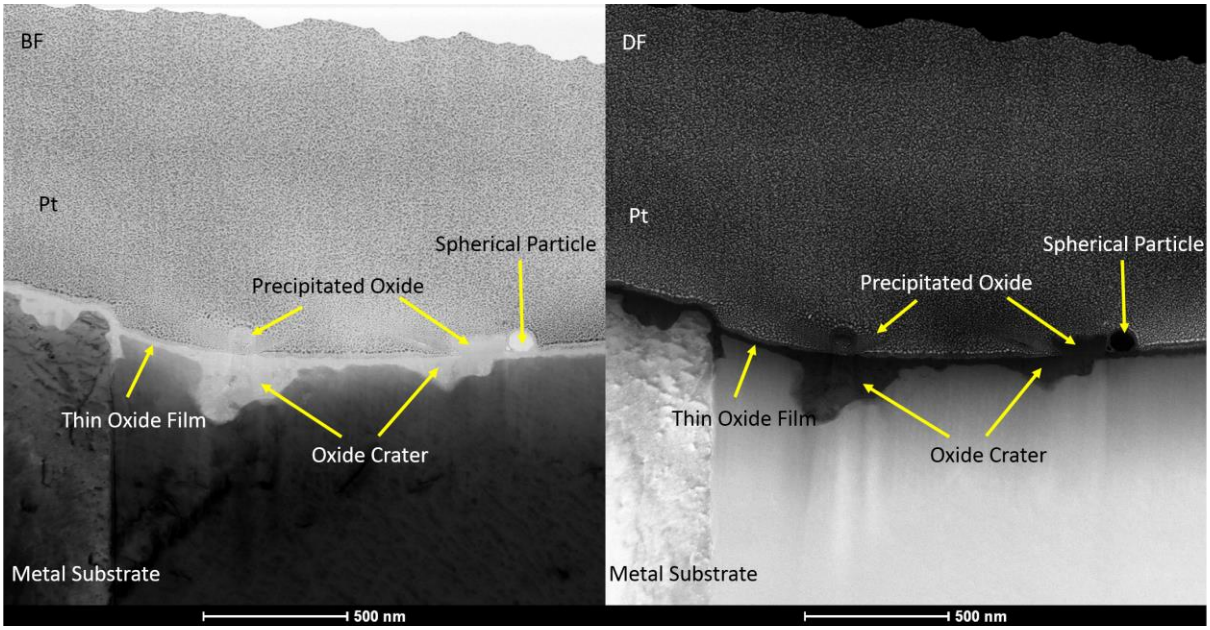

Figure 32 - STEM cross-section images (BF and DF) of the corroded surface of sample A1.

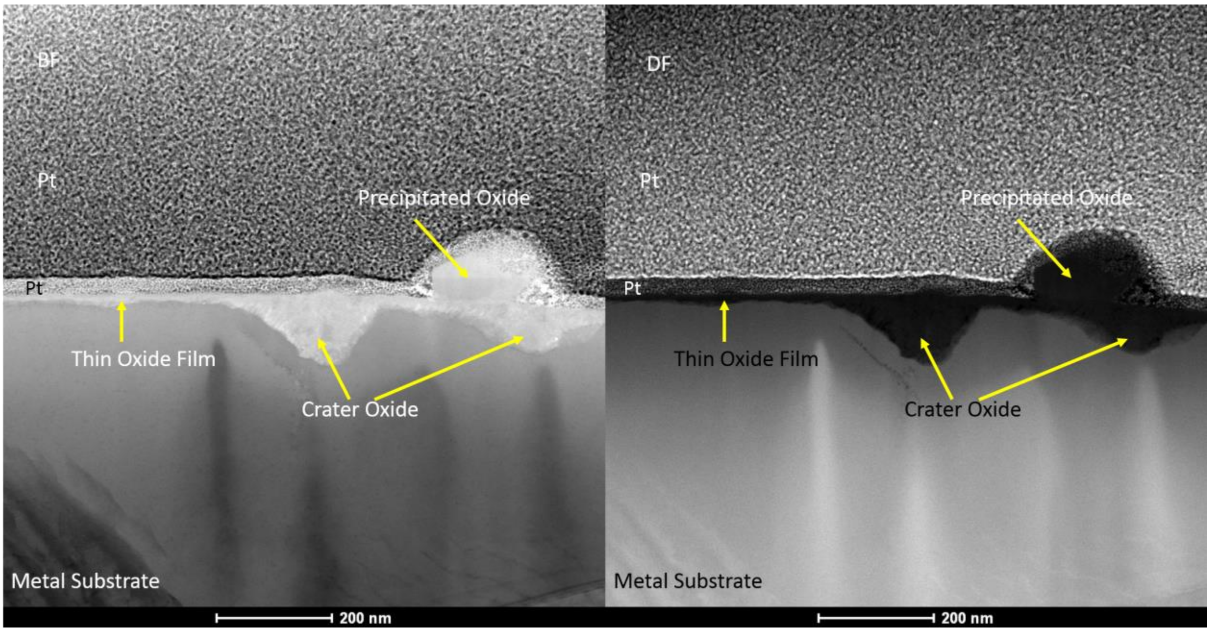

Figure 33 - STEM cross-section images (BF and DF) of the corroded surface of sample A1.

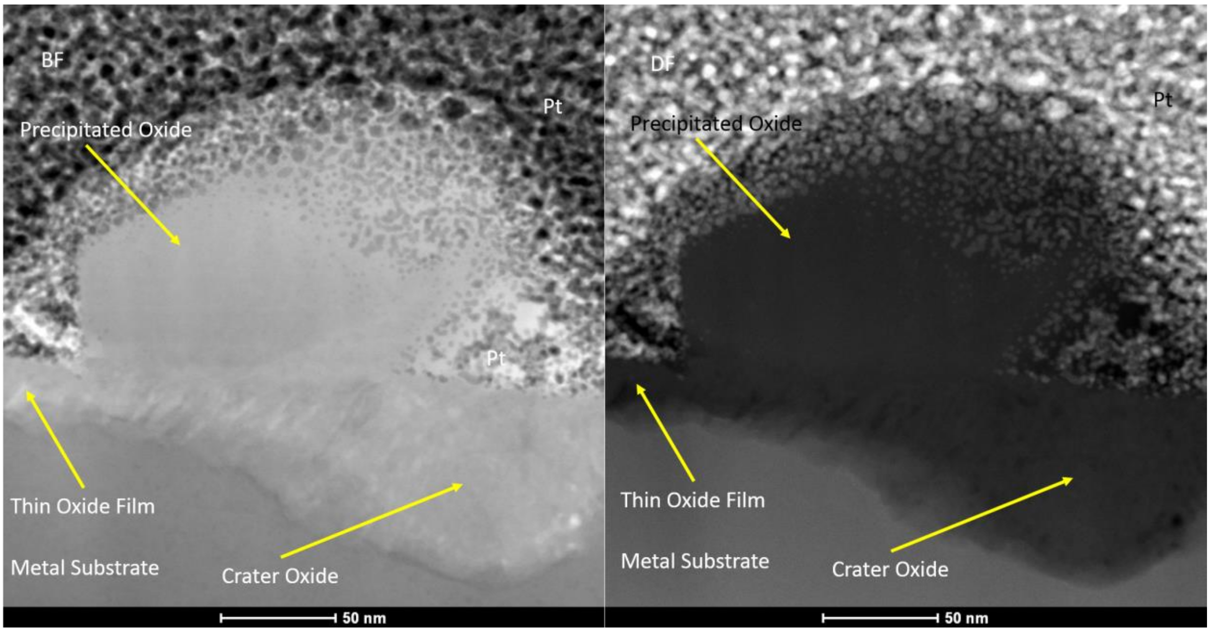

Figure 34 - STEM cross-section images (BF and DF) of the corroded surface of sample A1.

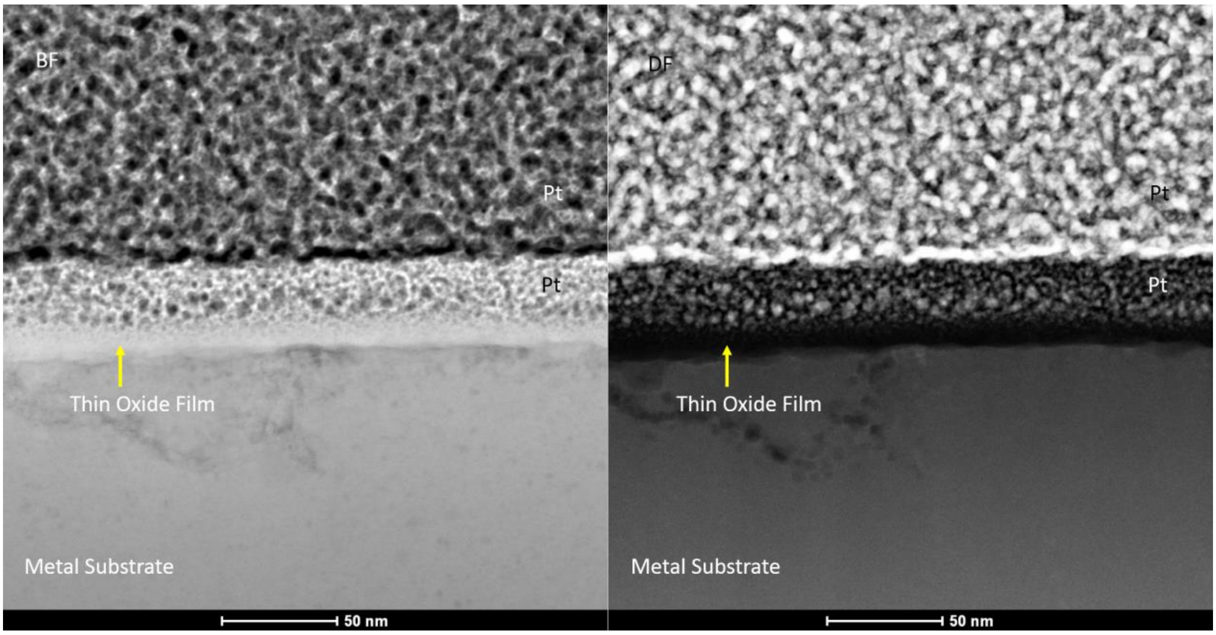

Figure 35 - STEM cross-section images (BF and DF) of the corroded surface of sample A1.

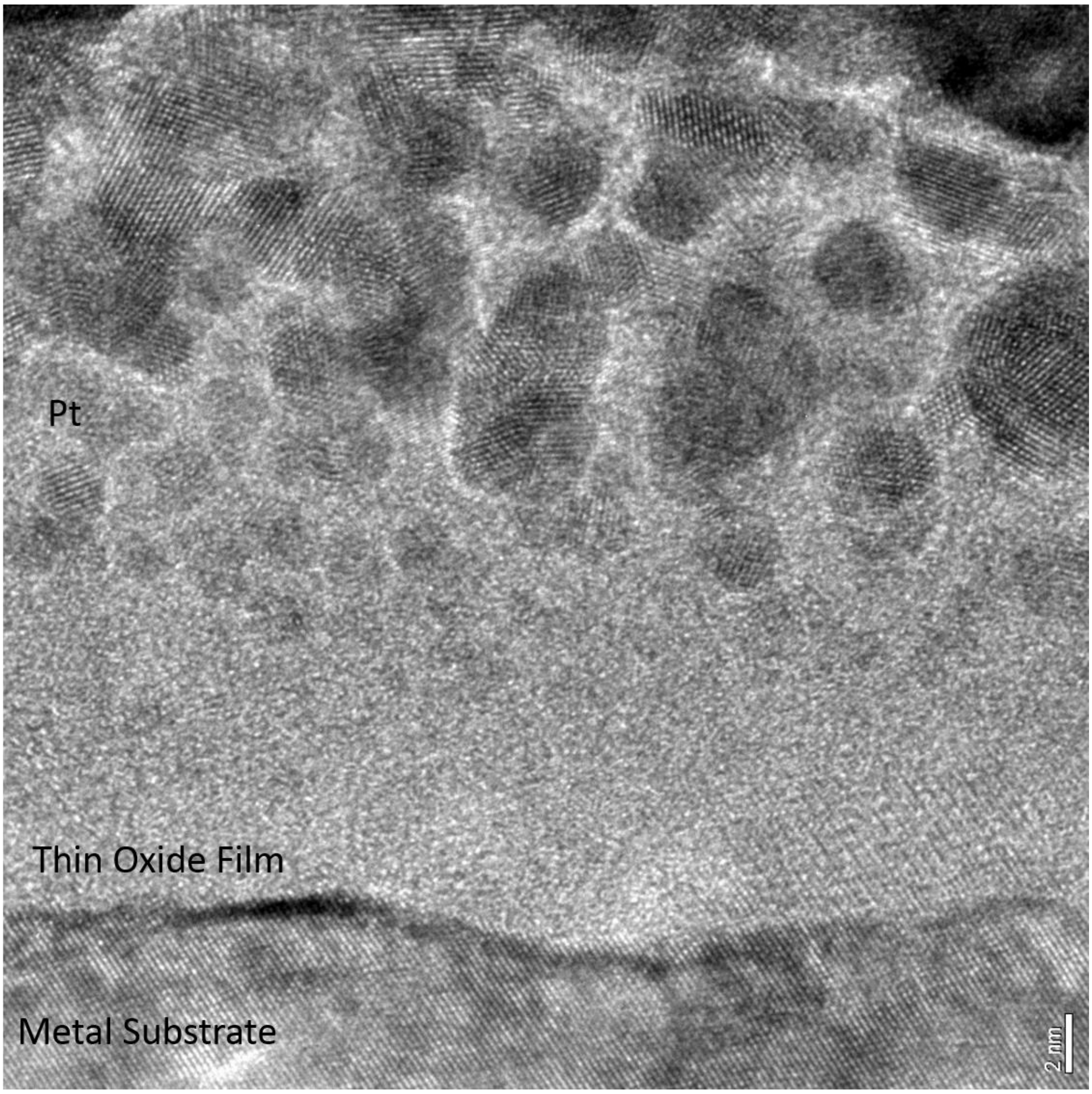

Figure 36 - HR TEM image of the thin oxide film of sample A1.

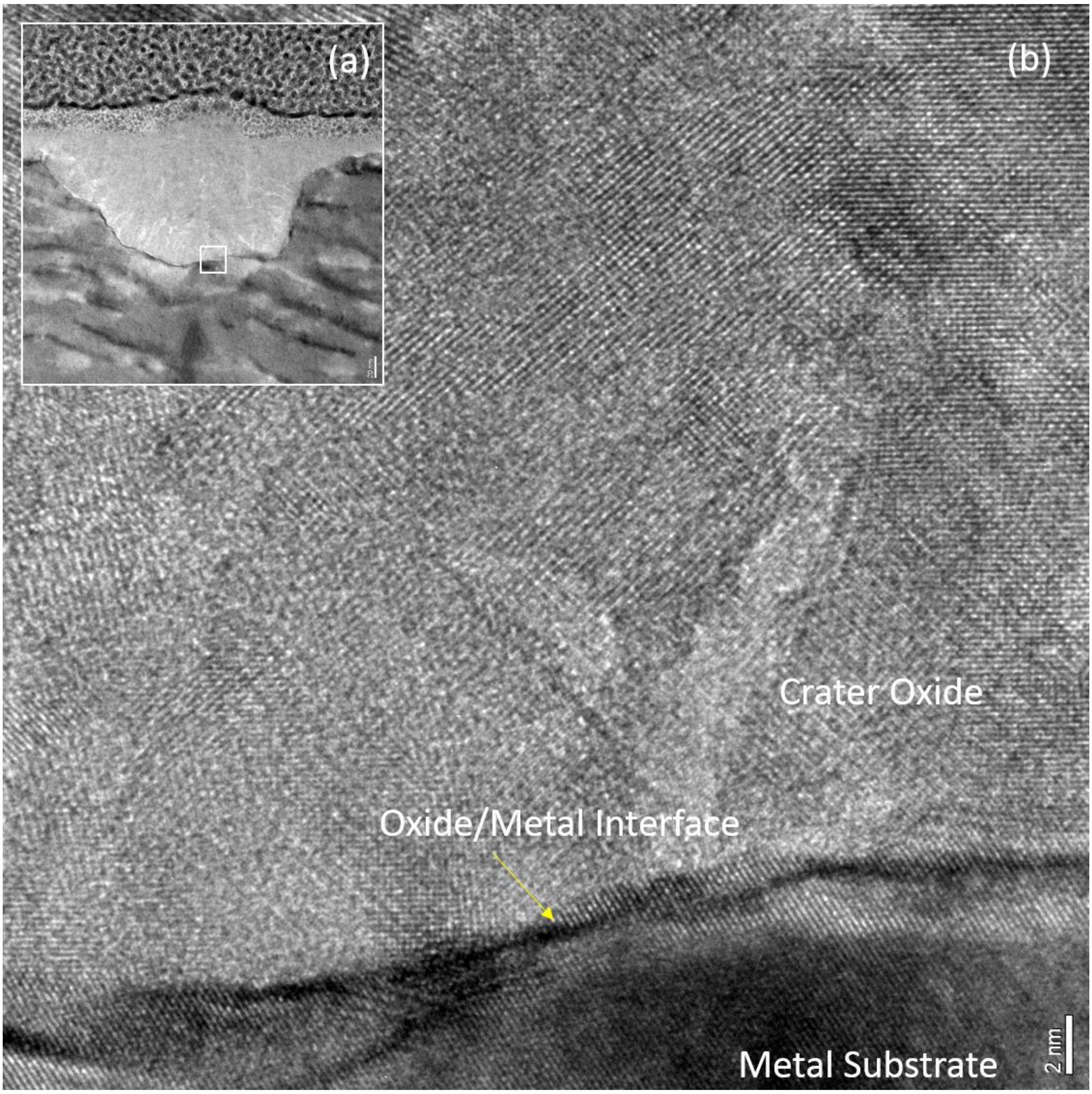

Figure 37 - HR TEM image of the oxide/metal interface region at the bottom of the crater oxide of sample A1.

Figure 38 shows the results of an EDS linescan measurement across a crater oxide region. One can see that the concentrations of the main oxide constituents (O, Fe, Ni, Cr and Mn) were constant across the crater oxide. A small fraction of zinc (approximately 1 at-%) could also be detected in the region close to the oxide surface. The zinc concentration profile across the thin oxide film is presented in Figure 39. One can see a concentration gradient of zinc in the oxide layer, summarised in Table 8. From area analyses at different sites in the dense precipitated oxide crystals, Figure 40, it is observed that no zinc is detected and the main elements are Fe, Ni and O. Regarding the spherical particles, Figure 41, the EDS measurements indicate the presence of Si and O. Since the measurement of oxygen is relatively uncertain, thus the ratio between the elements might not be exact, but the spherical particles seem to be silicon dioxide.

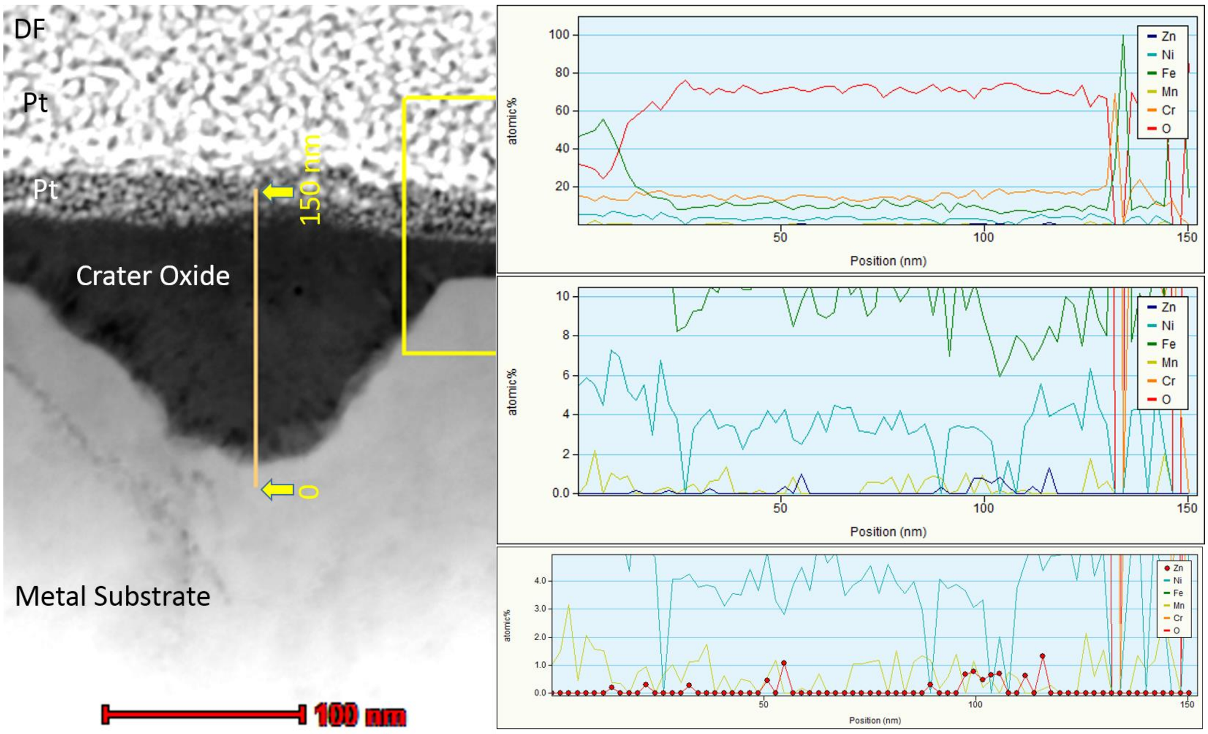

Figure 38 - Main elemental compositions (in at-%) across a crater oxide region. Three different scales for presenting elemental concentrations are used.

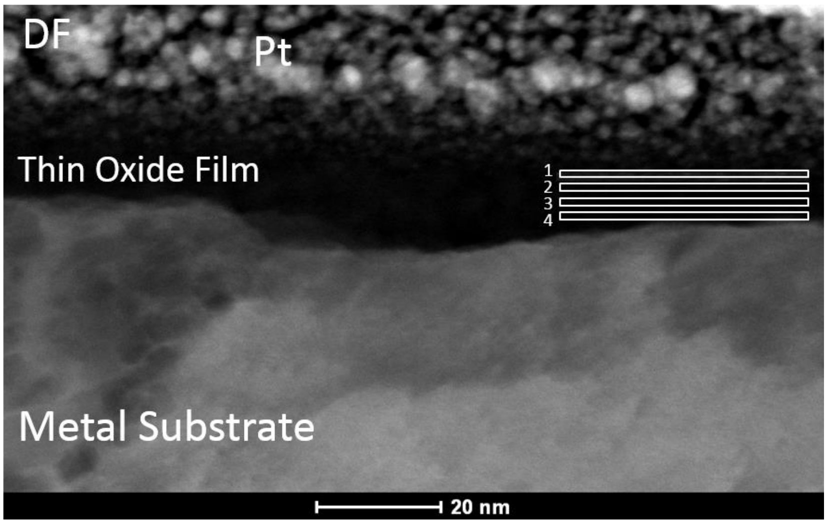

Figure 39 - Zinc concentration EDS measurement across a thin oxide film of sample A1.

Table 8 - Main elemental composition (in at-%) across a thin oxide film on sample A1.

Area	O	Si	Cr	Mn	Fe	Ni	Zn
1	53.9	1.4	22.7	1.4	13.9	6.1	0.7
2	45.4	1.0	24.1	2.4	16.7	9.5	1.0
3	37.8	1.2	19.0	1.3	27.2	12.9	0.6
4	23.7	0.9	17.5	2.1	40.5	15.1	0.3

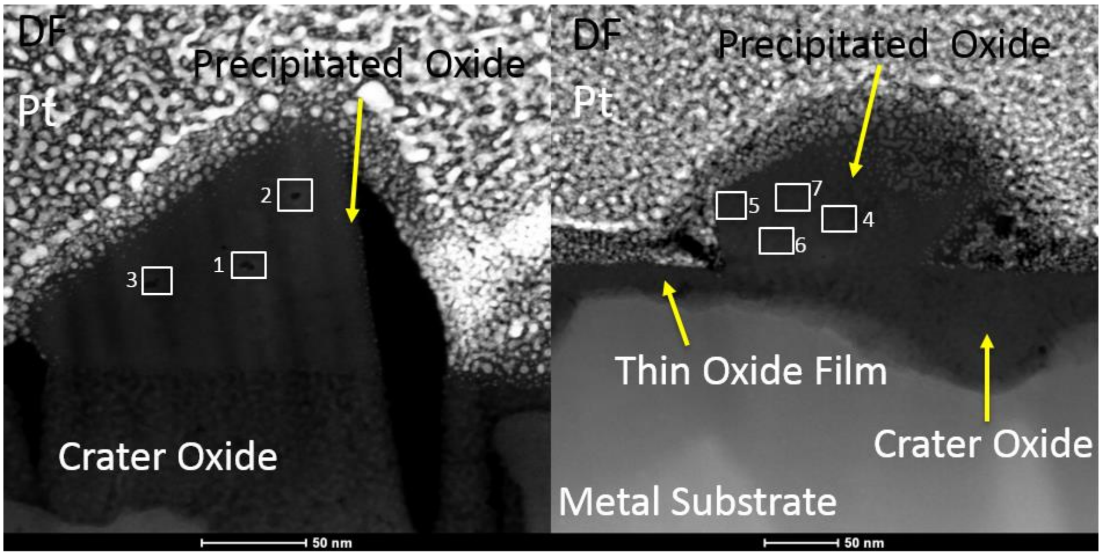

Figure 40 - EDS measurements on precipitated oxide grains on sample A1.

Table 9 - Main elemental composition (in at-%) in precipitated oxides on sample A1.

Area	O	Si	Cr	Mn	Fe	Ni	Zn
1	51.7	0.0	0.0	0.0	40.8	7.5	0.0
2	41.0	0.0	3.3	0.0	46.3	9.4	0.0
3	35.0	1.7	8.0	1.3	47.1	6.9	0.0
4	55.2	0.2	2.8	0.5	37.7	3.5	0.0
5	54.4	0.0	9.6	0.0	25.2	10.8	0.0
6	49.1	0.3	1.2	0.5	40.3	8.6	0.0
7	49.8	0.2	2.9	0.7	38.5	7.8	0.0

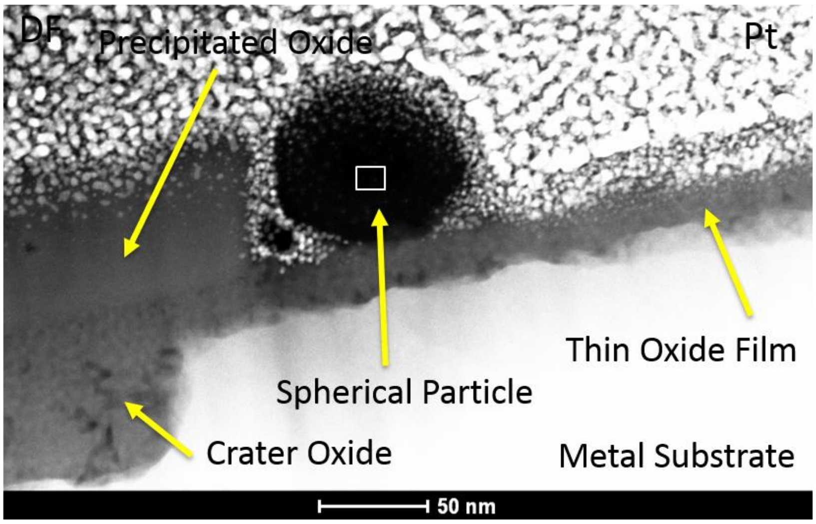

Figure 41 - EDS measurement on spherical particle on sample A1

Table 10 - Main elemental composition (in at-%) in a spherical particle on sample A1.

Area	O	Si
1	64	36

7.4.2 Cross-section microstructures of sample A3

Figure 42 to Figure 46 shows some TEM bright field (BF) and dark field (DF) images of a part of the cross-section of the TEM-lamella prepared from sample A3, in which the large precipitated oxide crystals, the small spherical particles, thin oxide film and crater oxides are indicated. HR TEM image of an interesting area is presented in Figure 47. Results from the elemental composition measurements are shown in Figure 48 to Figure 51 with corresponding data summarised in tables, Table 11 to Table 14.

The thickness of the thin oxide film was measured at 15 random locations. There were large variations (avoiding crater oxides and precipitated oxide grains), and the thickness was estimated to 38.5 ± 11.9 nm.

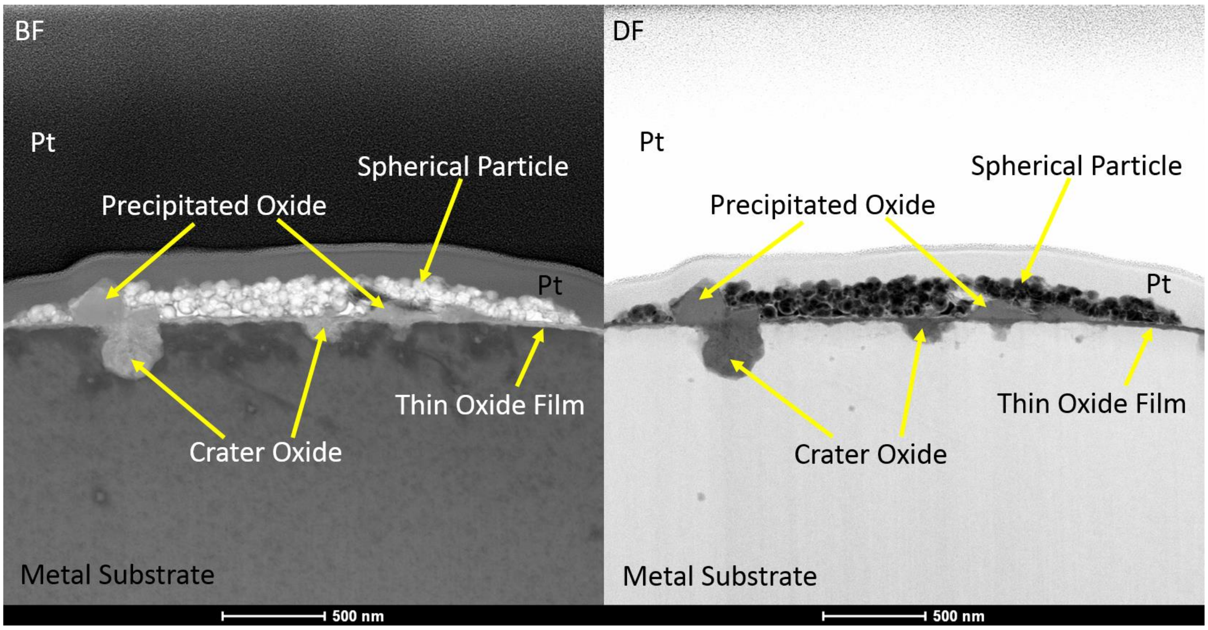

Figure 42 - STEM cross-section images (BF and DF) of the corroded surface of sample A3.

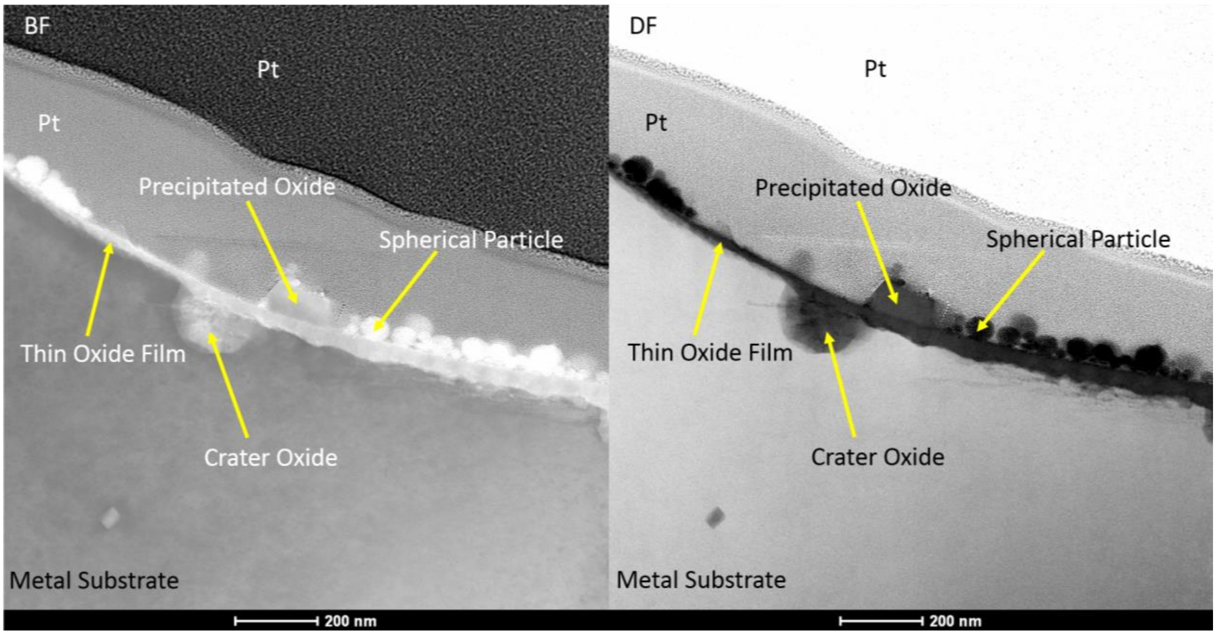

Figure 43 - STEM cross-section images (BF and DF) of the corroded surface of sample A3.

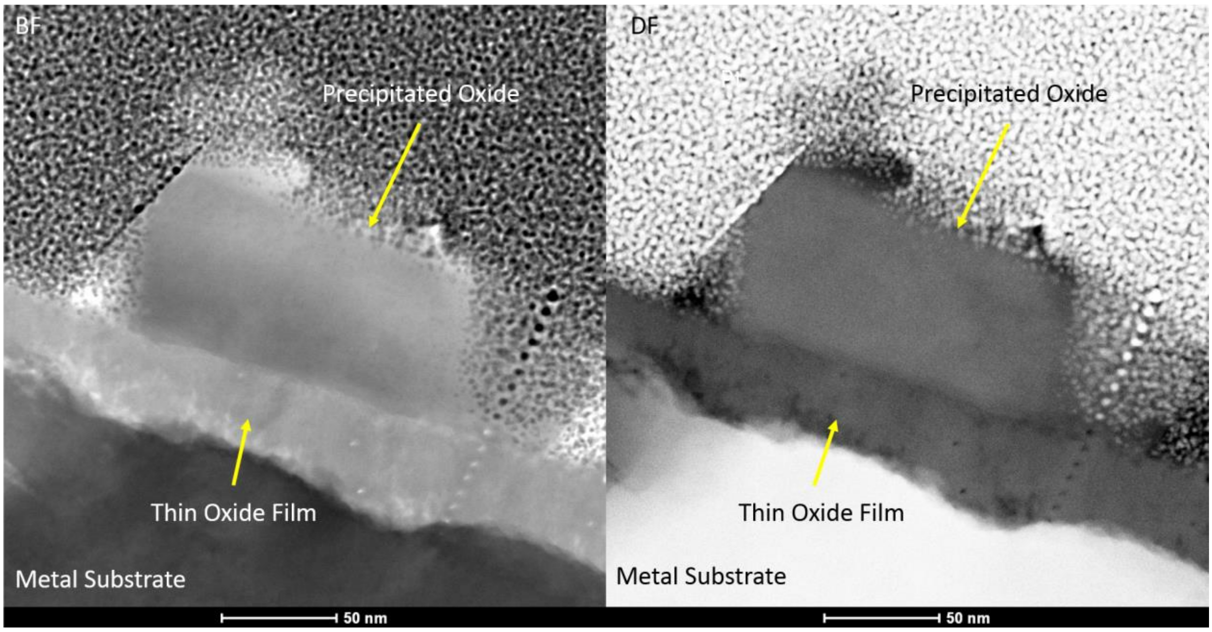

Figure 44 - STEM cross-section images (BF and DF) of the corroded surface of sample A3.

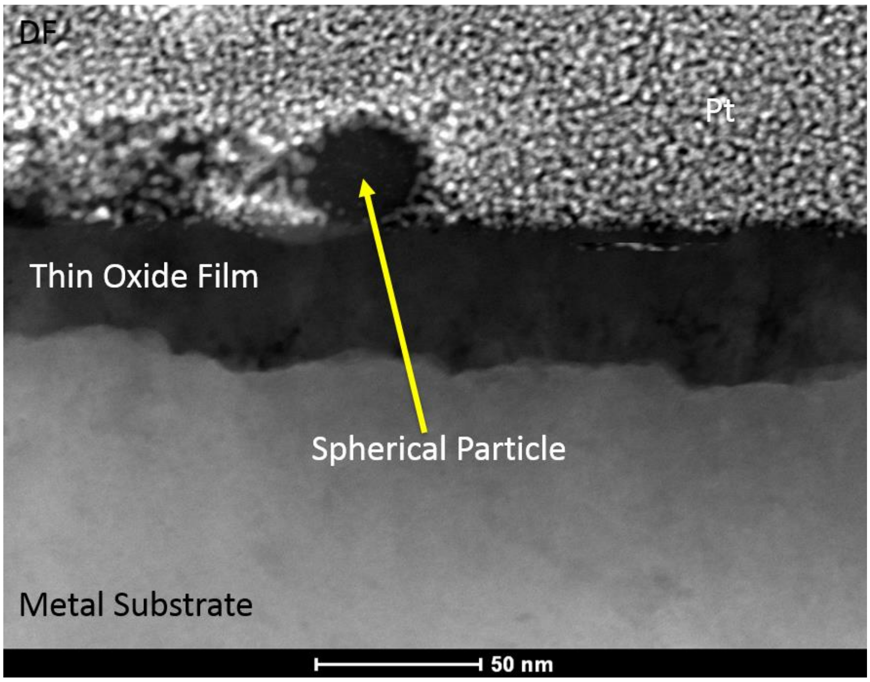

Figure 45 - STEM cross-section image (DF) of the thin oxide film of sample A3

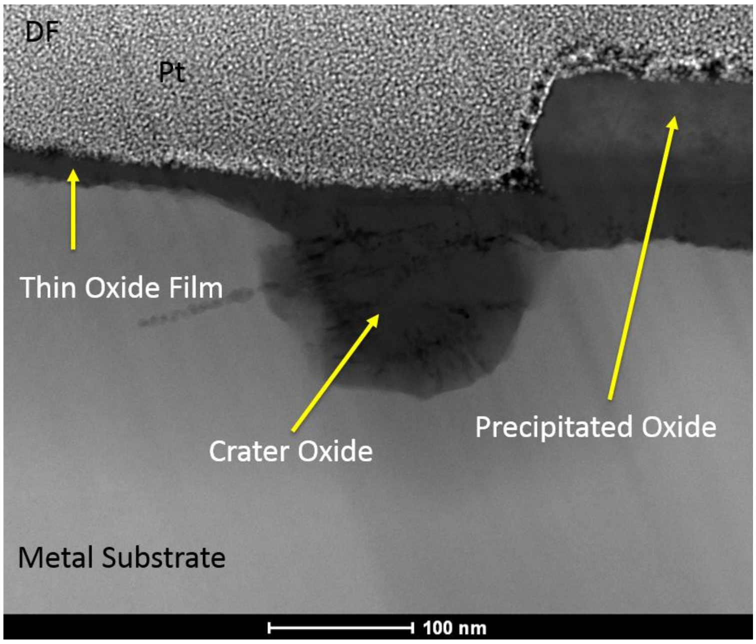

Figure 46 - STEM cross-section (DF) on crater oxide of sample A3.

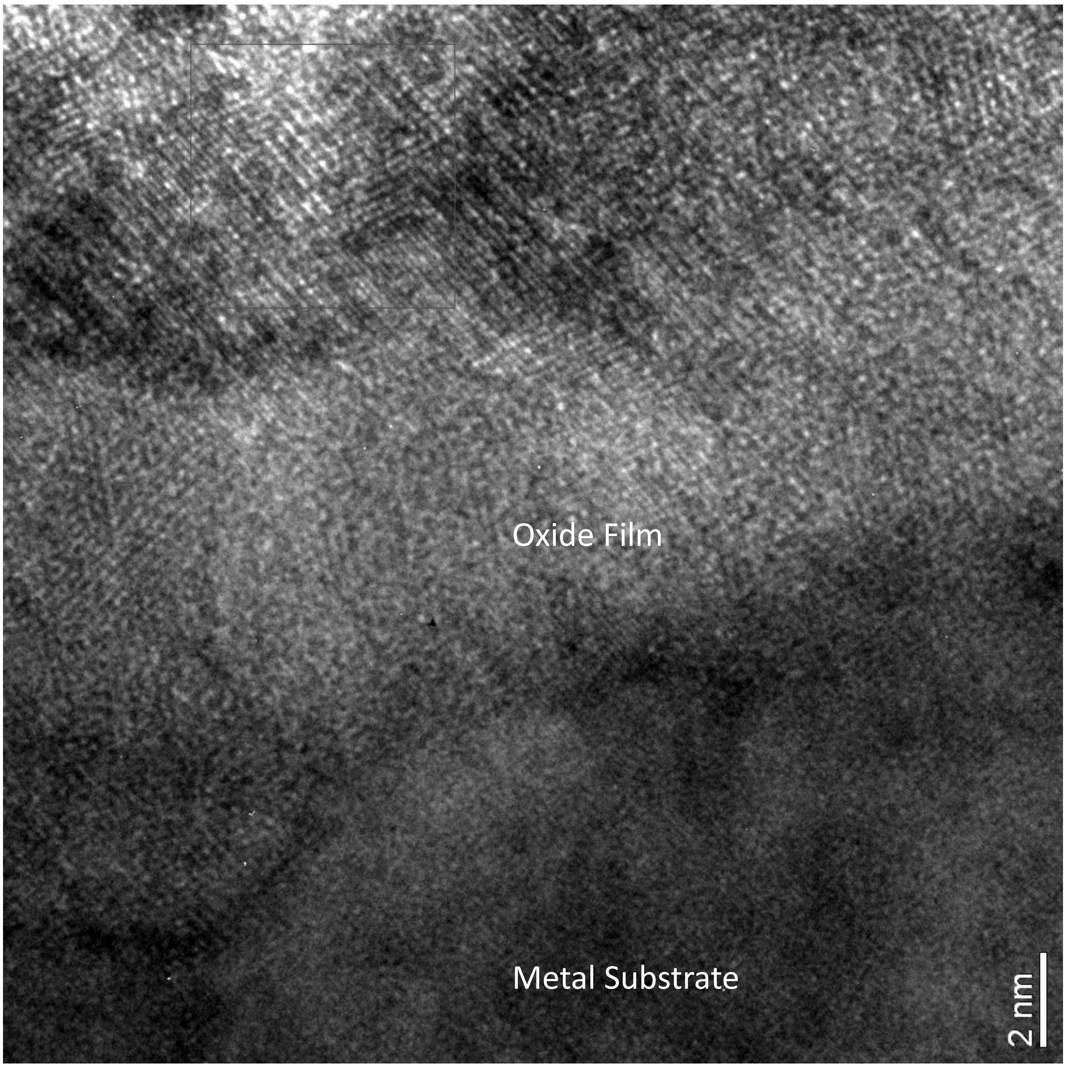

Figure 47 - HR TEM image of the oxide layer of sample A3.

Figure 48 shows the results of an EDS area scan measurement across the thin oxide film of sample A3. A zinc concentration gradient, maximum concentration of 1.1 at-%, can be observed from the top to the bottom of the thin oxide film, which can be viewed in Figure 48. It is also observed that the thin oxide film is Cr-rich. The EDS point analyses on a precipitated oxide crystal that have hollow structure, Figure 49, indicates on an elemental enrichment of Mn, Al, and Cr while the surrounding of the enrichment is Fe-rich, see Table 12, and no zinc is detected. EDS area scans across a crater oxide, Figure 50, show a zinc concentration gradient from the top into the middle of the crater. As seen in Table 13, the primary element in the oxide is Cr and the secondary elements are Fe, Ni and Mn. The presence of Si could be due to contamination.

EDS point analyses on spherical particles, Figure 51, resulted in Si and O containing particles, see Table 14. The ratio between Si and O is rather 1:1 than 1:2 as is the case of silicon dioxide. It is more likely that silicon dioxide has been formed than silicon monoxide, thus the uncertainty of the oxygen measurement could be the cause of the ratio difference.

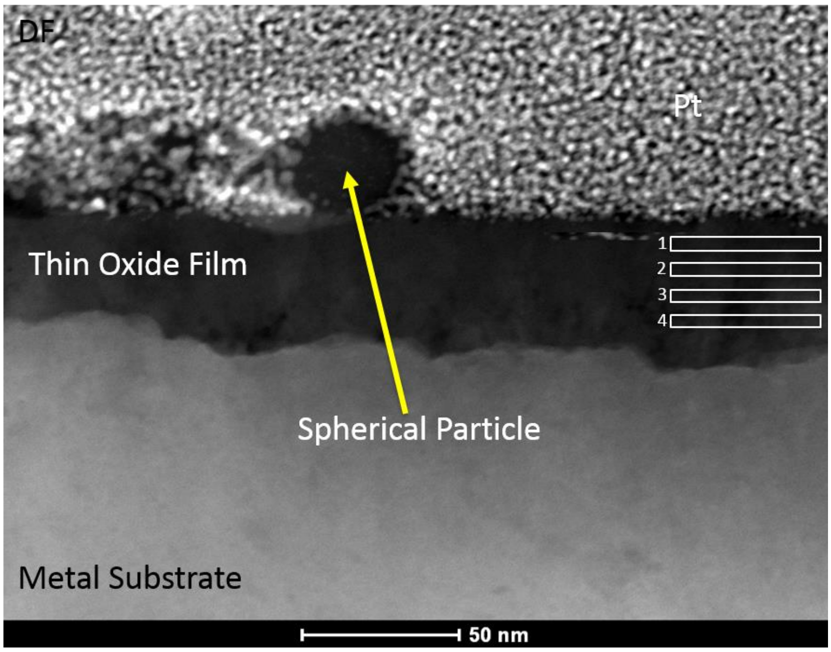

Figure 48 - Areas for elemental composition measurements across a thin oxide film on sample A3.

Table 11 - Elemental compositions (in at-%) of thin oxide film from EDS measurement (in at-%) on sample A3.

Area	O	Si	Cr	Mn	Fe	Ni	Zn
1	58.2	4.1	16.9	1.3	11.8	6.5	1.1
2	55.5	4.8	18.0	2.2	11.7	6.8	1.1
3	57.4	10.6	14.2	0.9	9.6	6.9	0.4
4	55.5	9.9	14.8	1.2	9.5	8.7	0.5

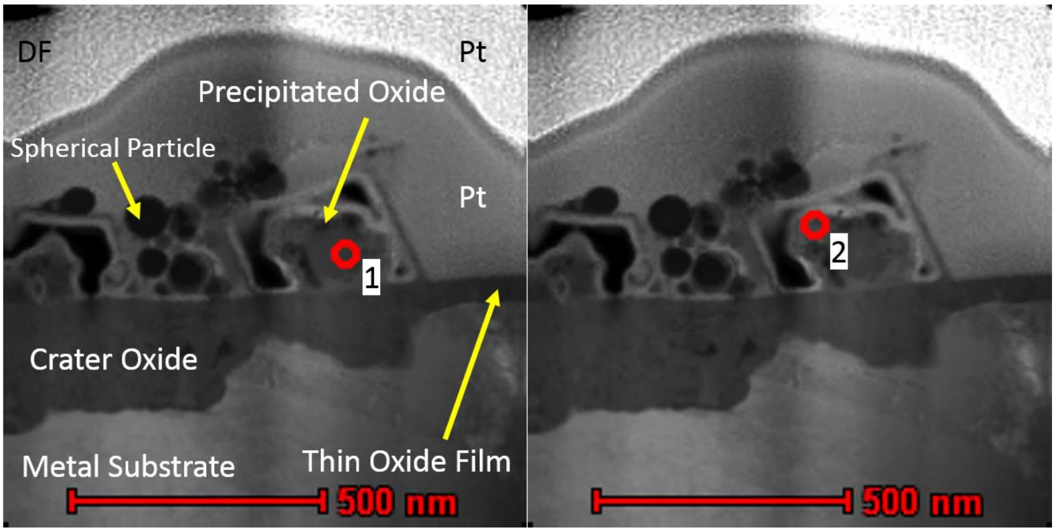

Figure 49 - Elemental composition measurement from different sites in precipitated oxide on sample A3

Table 12 - Elemental composition from EDS point analyses (in at-%) Figure 49 on sample A3.

Site	O	Al	Si	Cr	Mn	Fe	Ni	Zn
1	63.6	9.5	3.8	10.6	11.1	1.3	0.1	0.0
2	60.8	0.00	4.4	2.2	0.1	29.6	2.8	0.0

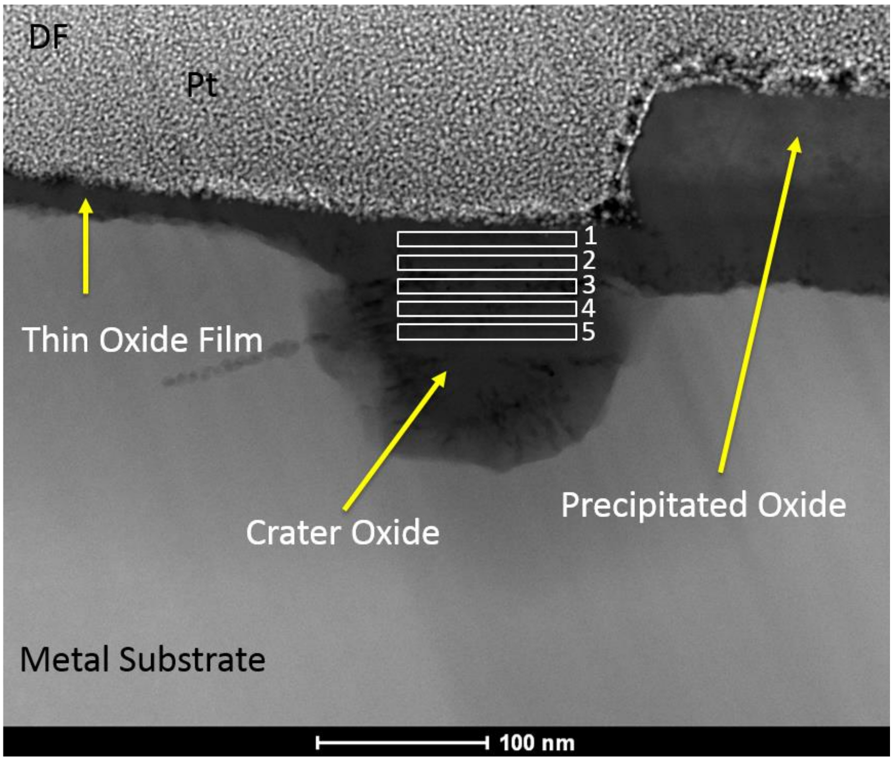

Figure 50 - Elemental composition measurement with areas across a crater oxide on sample A3.

Table 13 - Elemental composition (in at-%) in crater oxide on sample A3.

Area	O	Si	Cr	Mn	Fe	Ni	Zn
1	54.8	1.6	19.6	1.8	14.2	7.4	0.6
2	59.3	2.4	18.0	1.4	12.6	6.2	0.2
3	59.1	3.6	17.6	1.5	11.9	6.2	0.2
4	60.4	5.4	15.6	1.6	11.6	5.4	0.1
5	56.7	6.3	16.4	2.1	12.8	5.5	0.0

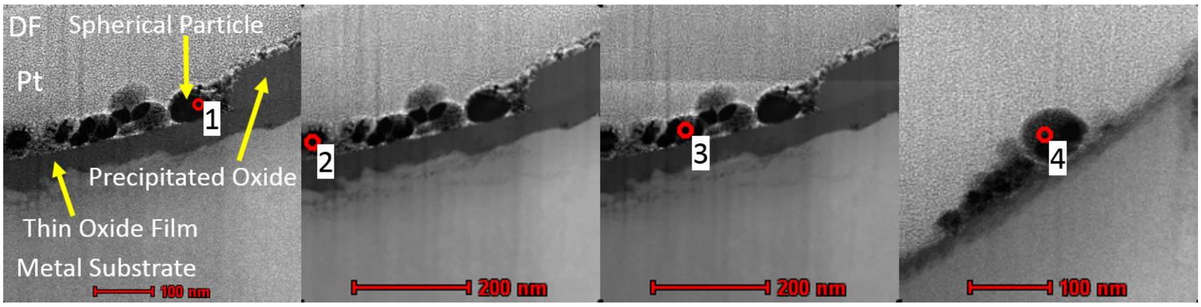

Figure 51 - Elemental composition measurement with point analyses on different spherical particles on sample A3.

Table 14 - Elemental composition in four spherical particles (in at-%) on sample A3.

Site	O	Si
1	55	45
2	59	41
3	55	45
4	56	44

7.4.3 Cross-section microstructures of sample B1

Figure 52 shows a TEM dark field (DF) image of a part of a cross-section TEM-lamella prepared from sample B1, in which the large precipitated oxide crystals, thin oxide film and crater oxides are indicated. The thin oxide film can be seen in Figure 53, to the left a STEM (DF) and to the right a TEM image. The oxide film thickness was measured at 20 random locations (avoiding crater oxides and precipitated oxide grains) and estimated to 23.5 ± 4.9 nm.

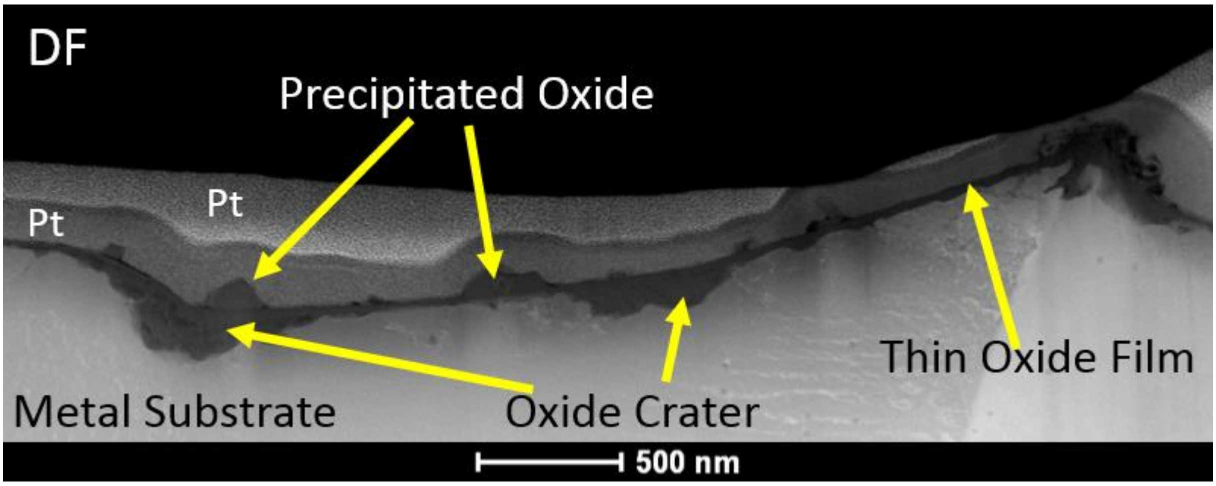

Figure 52 - STEM cross-section image (DF) of the corroded surface of sample B1.

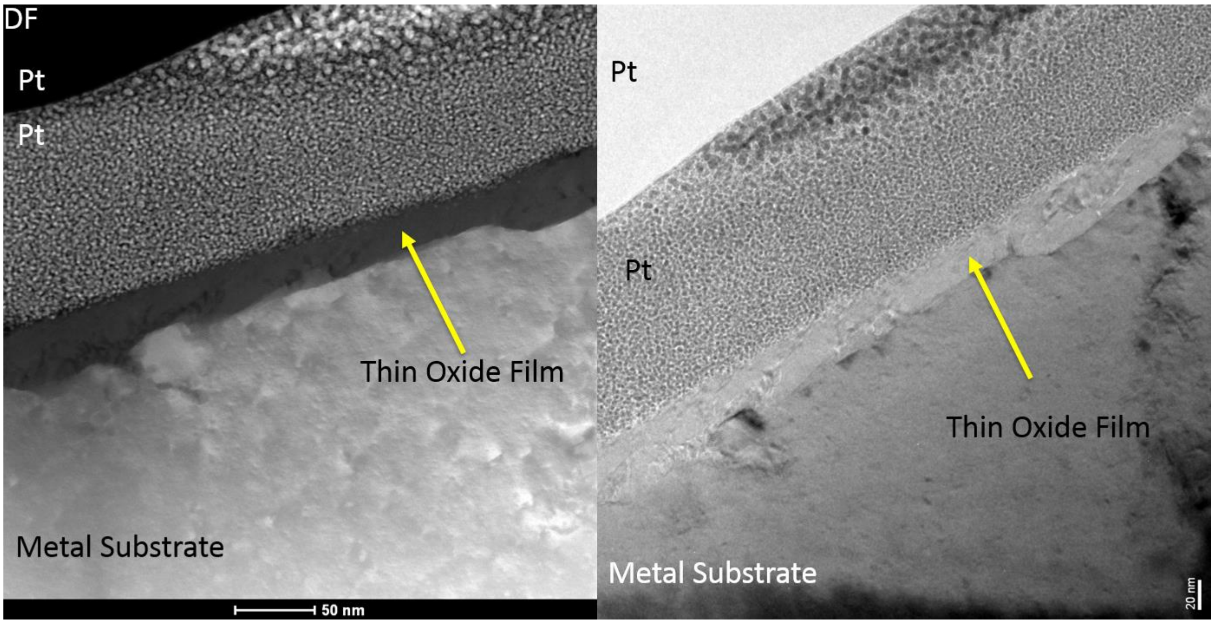

Figure 53 - Cross-section of sample B1 thin oxide film. Left image is STEM (DF), right image is TEM image.

7.4.4 Comparison between cross-section microstructures of samples A1, A3 and B1

Samples A1 and A3 have similar elemental compositions concerning their oxide features. The crater oxides are Cr-rich and have a zinc concentration gradient across the crater. There is also an observed zinc concentration gradient across the thin oxide films. Regarding the precipitated oxide crystals, two types exist, one with a dense structure and one with a hollow structure. The dense precipitated oxides are Fe and Ni-rich and the hollow precipitated oxides have an elemental enrichment of Mn, Al and Cr in the middle and are surrounded by a Fe-rich oxide.

The thin oxide films, on all samples, cover continuously the metal surface. A rough comparison between the samples thin oxide film thickness is that sample A1 (~16 nm) and B1 (24 nm) have more similar thickness while A3 (39 nm) is approximately twice as thick as the other two.

7.5 APPLICATION OF POINT DEFECT MODEL

As mentioned in Chapter 4, the original PDM-II [3] and that modified by Wu, et al. [29] do not treat the issue concerning radioactivity uptake in the oxide films. Nevertheless, the fundamental description regarding the duplex oxide layer formation and defect chemistry reactions across an oxide film is useful and can be readily modified to treat the presence of various radionuclides that are present in reactor primary coolant. For the type of corrosion products formed on the SS 304L as exposed for this study, the barrier oxide layer would be the thin oxide film and the crater oxide as described in Chapter 7.4, while the precipitates are the large oxide crystals. By following Wu's example in applying PDM in treating corrosion of stainless steel of type 304L, one can take both zinc and radiocobalt species in the coolant into consideration and rewrite the defect generation and annihilation reactions as shown in Figure 54. In this modified PDM reactions *k*, *l* and *m*, all of which include cobalt as a reactant, are added. In other words, zinc and cobalt species in the coolant play exactly the same role in replacing the metal cations (either M_M or $M_i^{\delta+}$) in the barrier oxide layer.

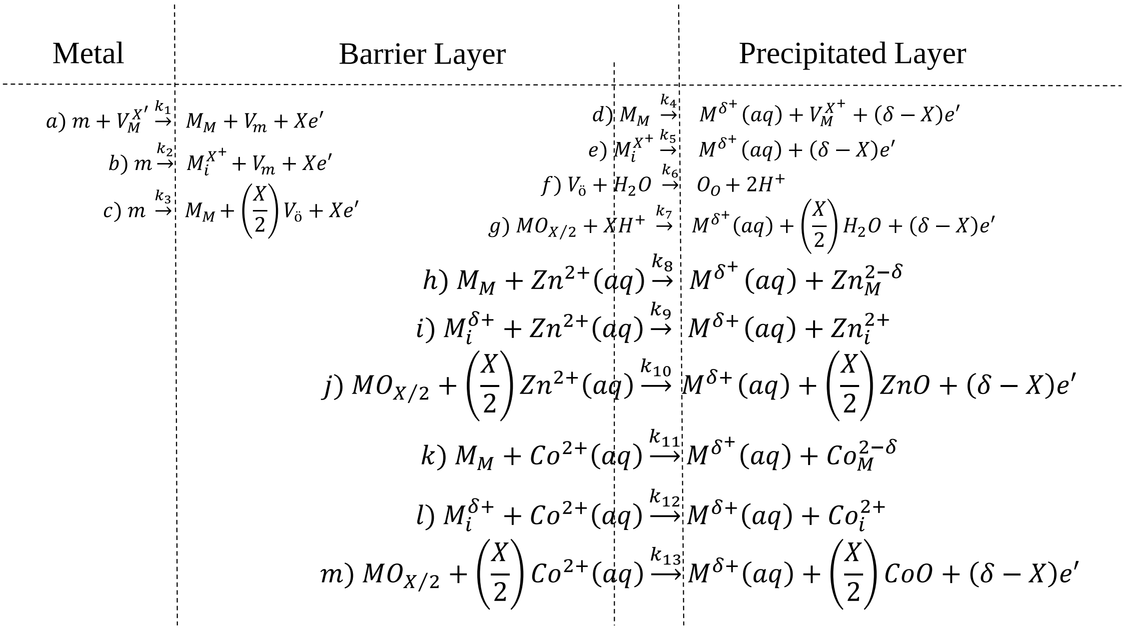

$$a)\ m + V_M^{X'} \xrightarrow{k_1} M_M + V_m + Xe'$$
$$b)\ m \xrightarrow{k_2} M_i^{X+} + V_m + Xe'$$
$$c)\ m \xrightarrow{k_3} M_M + \left(\frac{X}{2}\right) V_{\ddot{o}} + Xe'$$
$$d)\ M_M \xrightarrow{k_4} M^{\delta+}(aq) + V_M^{X+} + (\delta - X)e'$$
$$e)\ M_i^{X+} \xrightarrow{k_5} M^{\delta+}(aq) + (\delta - X)e'$$
$$f)\ V_{\ddot{o}} + H_2O \xrightarrow{k_6} O_O + 2H^+$$
$$g)\ MO_{X/2} + XH^+ \xrightarrow{k_7} M^{\delta+}(aq) + \left(\frac{X}{2}\right) H_2O + (\delta - X)e'$$
$$h)\ M_M + Zn^{2+}(aq) \xrightarrow{k_8} M^{\delta+}(aq) + Zn_M^{2-\delta}$$
$$i)\ M_i^{\delta+} + Zn^{2+}(aq) \xrightarrow{k_9} M^{\delta+}(aq) + Zn_i^{2+}$$
$$j)\ MO_{X/2} + \left(\frac{X}{2}\right) Zn^{2+}(aq) \xrightarrow{k_{10}} M^{\delta+}(aq) + \left(\frac{X}{2}\right) ZnO + (\delta - X)e'$$
$$k)\ M_M + Co^{2+}(aq) \xrightarrow{k_{11}} M^{\delta+}(aq) + Co_M^{2-\delta}$$
$$l)\ M_i^{\delta+} + Co^{2+}(aq) \xrightarrow{k_{12}} M^{\delta+}(aq) + Co_i^{2+}$$
$$m)\ MO_{X/2} + \left(\frac{X}{2}\right) Co^{2+}(aq) \xrightarrow{k_{13}} M^{\delta+}(aq) + \left(\frac{X}{2}\right) CoO + (\delta - X)e'$$

Figure 54 - Summary of the defect generation and annihilation reactions envisioned to occur at the interfaces of the barrier layer on a metal surface in a reactor coolant environment where various chemical species such as radiocobalt are present.

As Co and Zn, either as oxide constituents or as aqueous species, are slightly different from each other in many chemical and physical properties, it is anticipated that the reaction rates k_{11}, k_{12} and k_{13} involving cobalt are different from the rates for the similar reactions but involving zinc (k_8, k_9 and k_{10}). In replacing the metal cations (either M_M or $M_i^{\delta+}$) in the barrier oxide layer, both zinc and cobalt would compete on the same species/sites of the barrier oxide layer at the oxide/solution interface. In other words, the presence of zinc in the coolant would decrease the chemical reaction rates between cobalt species in the coolant and the metal cations (either M_M or $M_i^{\delta+}$) in the barrier oxide layer, and *vice versa*. This would in a simple way explain why zinc injection would decrease radiocobalt incorporation in the oxide films. It could also explain the experimental observation [12] that zinc injection accelerated the radiocobalt release from the corroded metal surfaces when injection of radiocobalt in the coolant was stopped. In such a case, the continuous presence of zinc in the coolant would replace the radiocobalt cations that have already been incorporated in the oxide films in a similar fashion as it replaces the other metal cations (either M_M or $M_i^{\delta+}$) in the barrier oxide layer.

An important conclusion from PDM is that the barrier layer contains only those species that are present in the metal and not those species in the aqueous solution. Apparently, this conclusion is not in agreement with the facts regarding the presence of zinc in the barrier layer in Wu's study [29] and in this study. The implication of such a disagreement between the model and the experimental facts remains unclear at present.

8. CONCLUSIONS

Based on the experimental examinations in this work, the following conclusions may be drawn:

1) All oxide films have duplex layer structures, with an outer oxide layer consisting of relatively large Ni-, Fe-, Cr-containing oxide crystals, small spherical silicon oxide particles, and an inner thin (~20 nm) Cr-rich oxide film and crater oxides.
2) The oxides on sample A1 contain slightly lower Cr content than in sample A3 and sample B1. Accordingly, the oxides in sample A1 have a slightly higher Ni content than in sample A3 and sample B1. The Fe contents of oxides in all samples are similar.
3) High resolution TEM images were obtained for the oxide films on samples A1, A3 and B1, providing a number of interesting microstructural details.
4) Zinc concentration gradients within the thin oxide films and the crater oxides in samples A1 and A3 have been determined and confirmed, up to ~1 at-% zinc was detected on the very surfaces.
5) No zinc was detected in the precipitated oxide crystals of samples A1 and A3.
6) A modified PDM is proposed to explain the competing mechanisms between zinc and cobalt in the reactor coolant in replacing metal cations on the surfaces of oxide films.

9. SUGGESTIONS FOR FUTURE WORK

The measured zinc concentrations have been up to 1 at-% from the TEM/EDS measurement, a complementing analysis technique that might be a suitable choice for this purpose could be Atom Probe Tomography. The technique uses an electric pulse through an atom probe tip, made from the sample that will eject the outermost atom layer that is collected by a time-of-flight detector. With right parameters, this technique might provide a 3D micrograph of the oxide film which could give a more precise indication of where zinc is present within the thin continuous oxide film or in the inward growing crater oxides.

Another analysis technique that might be considered for this purpose of detecting low concentrations of zinc could be Time of Flight Secondary Ion Mass Spectroscopy, where the oxide is sputtered with ions and then detected by a time-of-flight detector for determining the detected ions.

ACKNOWLEDGEMENTS

I would like to direct my greatest gratitude to Adjunct Professor Jiaxin Chen for giving me this opportunity to perform my master's thesis involving everything that I ever wanted from a thesis work, valuable experiences regarding different analytical techniques, very insightful discussions and for being an excellent supervisor.

I would like to thank Studsvik Nuclear AB for providing all studied samples and Ringhals AB for partial financial support.

I would like to thank my supervisors Professor Krystyna Stiller and Doctor Mattias Thuvander for all interesting discussions and valuable feedback

A special thanks to Doctor Stefan Gustafsson and Doctor Henrik Pettersson for operating TEM and performing the TEM analyses

A special thanks to Mr. Yuan-Chih Lin and Doctor Habibur Rahman for being excellent supervisors regarding Laser Raman Spectroscopy and X-Ray powder Diffraction, respectively

A special thanks to Professor Mats Halvarsson for valuable advices regarding EDS analyses

A special thanks to Ms. Kristina Lindgren, Mr. Amine Yousfi and Doctor Torben Boll for supervising SEM and FIB-SEM, respectively

A special thanks to Doctor Anders Kvist for supervising and sharing valuable experiences regarding the electron microscopes and to Ola Löfgren for it-support

I also want to say thanks to all of you taking your time answering my hundreds of questions

Cecilia Fager, Gothenburg 2015-06-18

REFERENCES

1. Hoffelner, W. (2013) *Materials for Nuclear Plants: From Safe Design to Residual Life Assessments*: Springer.

2. *Radionuclide saftey data sheet - Co58 and Co59*, Stanford, Editor.

3. Macdonald, D.D. (2012) The Passive State in Our Reactive Metals-Based Civilization. *Arabian Journal for Science and Engineering*, vol. 37, pp. 1143-1185.

4. Authority, S.R.S. (2013) Performance of a Pressurized Water Reactor.

5. Green, S.J. (1995) PWR steam generators. *International Journal of Multiphase Flow*, vol. 21, p. 2.

6. Féron, D., Herms, E. (2012) Behavior of stainless steels in pressurized water reactor primary circuits. *Journal of Nuclear Materials,* vol. 427, no.1–3: pp. 364-377.

7. Jones, A. (1996) Principles and Prevention of Corrosion. pp. 515-517.

8. Davis, J.R. (2001) Alloying: Understanding the Basics, *ASM International*, pp. 257-261.

9. Zahner, L.W. (1995) Architectural Metals: A Guide to Selection, Specification, and Performance. p. 206.

10. Hicks, J.H. (2000) Nuclear Reactors, Water Chemistry of Lightwater Reactors, *Kirk-Othmer Encyclopedia of Chemical Technology*. John Wiley & Sons, Inc.

11. Bengtsson, B., Aronsson, P-O., Larsson, S., Andersson, P-O. Experiences with Elevated pH and Lithium in Ringhals PWRs.

12. Öijerholm, J., Gillén, P., Chen, J. (2013) Examination of Radioactivity Uptake on PWR Reactor Materials by Using Radiotracer Technique - Steam generator cold leg conditions at pH300 7.1 w/wo Zn injection.

13. Liu, X., Wu, X., and Han, E-H. (2011) Influence of Zn injection on characteristics of oxide film on 304 stainless steel in borated and lithiated high temperature water. *Corrosion Science*, vol. 53, no. 10, pp. 3337-3345.

14. Tapping, R.L., et al. (1986) The composition and morphology of oxide films formed on type 304 stainless steel in lithiated high temperature water. *Corrosion Science*, vol. 26, no. 8, pp. 563-576.

15. Lesley, E. S. (2012) Solids State Chemistry: An Introduction. pp. 75-81.

16. Larkin, P. (2011) Infrared and Raman Spectroscopy Principles and Spectral Interpretation*:* Elsevier.

17. Harris, D. C. (1978) Symmetry and Spectroscopy An Introduction to Vibrational and Electronic Spectroscopy: Oxford University Press.

18. Bielecki, J. (2012) *Structure and dynamics in transition metal perovskites - an optical spectroscopy study*. Gothenburg: Chalmers University of Technology. pp. 52-53. (Doctoral Thesis at the Department of Applied Physics)

19. Kumar, C. S. S. R. (2012) Raman Spectroscopy for Nanomaterials Characterization. p. 593.

20. Goldstein, J., et al. (2003) Scanning Electron Microscopy and X-Ray Microanalysis. pp. 23, 75, 88, 274: Springer

21. Lesley E. S. (2012) Solids State Chemistry : An Introduction. pp. 102-103, 107.

22. Facility, A.M.a.M.R (2013) Scanning Electron Microscope Training Module. http://www.ammrf.org.au/myscope/sem/background/concepts/interactions.php. (2015-05-03).

23. Facility, A.M.a.M.R. (2013) Energy Dispersive X-Ray Spectroscopy. http://www.ammrf.org.au/myscope/analysis/eds/#term. (2015-05-04).

24. Giannuzzi, L. A., Stevie, F.A. (2005) Introduction to Focused Ion Beams: Springer.

25. Williams, D. B., Carter, C. B. (2009) Transmission Electorn Microscopy: Springer.

26. Öijerholm, J., Gillén, P. (2013) Examination of Radioactivity Uptake on PWR Reactor Materials by Using Radiotracer Technique - Steam generator hot leg conditions at pH300 7.4 w/wo Zn injection.

27. Graves, P. R., et al. (1988) Raman Scattering In Spinel Structure Ferrites. *Materials Research Bulletin*, vol. 23, no. 11, pp. 1651-1660.

28. De Faria, D. L. A., Silva, S. V. (1997) Raman Microspectroscopy of Some Iron Oxides and Oxyhydroxides. *Jounral of Raman Spectrocospy*, vol. 28, pp. 873-878.